nature biomedical engineering

Article

https://doi.org/10.1038/s41551-026-01743-2

Super homotypic targeting by surface engineering of extracellular vesicles

Received: 21 November 2024

Accepted: 12 June 2026

Published online: 22 July 2026

Check for updates

Huai-Song Wang[1,2,26], Tianben Ding[1,3,4,26], Yuhong Liu[1,26], Fabio Lisi[1], Yuqi Zhou[1], Yaqi Zhao[1], Xin-Yuan Hu[2], Zi-Wei Yang[2], Jing-Lian Su[2], Mika Hayashi[1], Natsumi Tiffany Ishii[1], Hiroki Matsumura[1], Anel Umirbaeva[5], Hongwei Guo[1,6], Yin-Yu Yan[2], Fu-Han Gao[2], Jia-Jing Li[2], Yasutaka Kitahama[1], Petra Paiè[7], Ayumi Taguchi[8], Kenbun Sone[8], Yuka Inoue[9], Takayuki Ueno[9], Abdullah N. Alodhayb[10], Nao Nitta[11], Masako Nishikawa[12], Yutaka Yatomi[12], Hiroyuki Matsumura[1], Ya Ding[2], Masahiro Sonoshita[13,14], Dino Di Carlo[15,16,17,18], Shiro Suetsugu[19,20,21,22] & Keisuke Goda[1,3,4,11,13,15,23,24,25]

Homotypic targeting is the inherent ability of cells to preferentially interact with cells of the same type, a phenomenon seen in cell adhesion, tissue formation and immune responses. However, its potential remains underexploited. Here we report a strategy to substantially enhance homotypic targeting through extracellular vesicles secreted by cells. By engineering the surface of small extracellular vesicles (sEVs) with lanthanides, we amplify specific cell–sEV interactions by more than 25-fold, enabling the selective capture of sEVs by cells of the same lineage even in the presence of excess off-target sEVs. We term this effect 'super homotypic targeting'. Super homotypic targeting provides a means to distinguish sEVs of different origins within highly heterogeneous sEV populations and enables two applications: using cells to detect specific sEVs and using sEVs to detect specific cells, specifically demonstrated here in the context of cancer detection from blood samples. Super homotypic targeting could hold potential for diagnostics, immunotherapy, drug delivery, rejuvenation and tissue engineering.

Homotypic targeting is a fundamental biological concept where cells preferentially interact or bind with cells of similar or identical types[1–5]. This homophilic specificity is crucial in various physiological processes, including cell adhesion, tissue formation and immune responses[6–10]. In therapeutic development, especially in targeted drug delivery, homotypic targeting is important in ensuring that drugs are delivered primarily to target cells, reducing systemic side effects and increasing treatment efficacy[5,11–14]. Furthermore, in tissue engineering, homotypic targeting facilitates the controlled interaction and formation of tissues by cells[15,16]. In the field of immunology, it is pivotal in enabling T cells to engage in homotypic interactions during the formation of immunological synapses, which are essential for mounting effective immune responses[17,18]. Nonetheless, the full potential of homotypic targeting remains largely untapped, mainly owing to challenges in achieving high specificity, fast responses and preventing off-target effects in complex and heterogeneous conditions such as cancer[1,11,13,14].

In this study, we introduce an approach to drastically boost the homotypic targeting capabilities of cells via extracellular vesicles secreted by cells. By engineering the surface of small extracellular vesicles (sEVs), typically ranging from 30 to 150 nm in diameter, with lanthanide ions such as Eu^{3+} and Tb^{3+} (Fig. 1a), we leverage the natural overexpression of sialic acid (SA) residues on cell membranes, a common characteristic in cancer cells[19–21], for competitive coordination with these lanthanide ions. Unlike previous sEV modification

A full list of affiliations appears at the end of the paper. e-mail: goda@chem.s.u-tokyo.ac.jp

https://doi.org/10.1038/s41551-026-01743-2

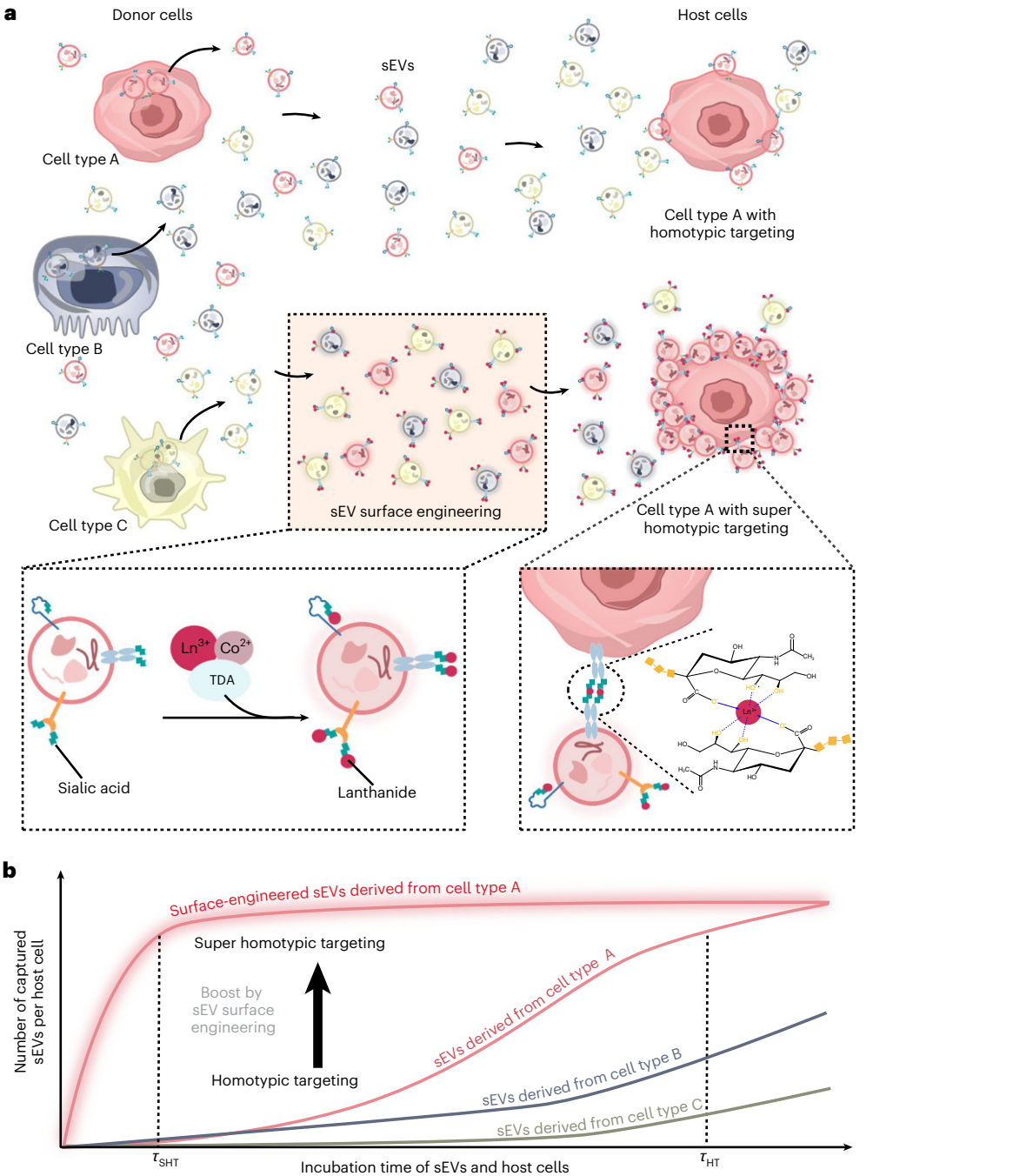

Fig. 1 | Concept of super homotypic targeting. a, A schematic illustration of the super-homotypic-targeting concept. The homotypic targeting capabilities of host cells (type A) are substantially boosted by engineering sEV surfaces with lanthanide ions. **b**, The sEV capture rates of host cells (type A) when incubated in a pool of sEVs from various donor cells (types A–C). sEV surface engineering amplifies specific cell–sEV interactions, thereby substantially speeding up the selective capture of sEVs by cells of the same lineage (type A), even in the excessive presence of sEVs from other cell types (type B and type C). This amplification dramatically reduces the sEV capture time of the host cells ($\tau_{SHT} \ll \tau_{HT}$), offering a distinct strategy for discriminating sEVs from different origins in the heterogeneous population of sEVs. In other words, host cells can act as selective instruments for distinguishing between various sEV types, on the basis of their capture speed.

techniques that involve directly loading nanomaterials onto sEVs to impart additional functions (for example, magnetic nanoparticle-based hyperthermia)[22,23], our lanthanide-coordination strategy dramatically amplifies cell–sEV inherent interactions by more than 25-fold. This enhancement substantially accelerates the selective capture of sEVs by cells of the same lineage, even in the excessive presence of other sEV populations (Fig. 1a). This amplification, which we refer to as 'super homotypic targeting', is not just a marginal improvement but a substantial enhancement in homotypic targeting efficiency. It reduces the sEV capture time of the cells from more than 2 days to only about 3 h, offering a practical strategy for discriminating sEVs from different origins in a highly heterogeneous population of sEVs (Fig. 1b). In other words, cells can act as selective instruments for distinguishing between various sEV types, based on their capture speed. Consequently, this substantial enhancement in sEV-mediated cellular homophilicity opens up an entirely distinct class of applications, two notable examples of

which we showcase here: using cells to detect specific sEVs and using sEVs to detect specific cells. The concept of 'super homotypic targeting' holds potential for cancer diagnostics, immunotherapy, drug delivery, rejuvenation and tissue engineering.

Surface engineering of sEVs

To experimentally demonstrate super homotypic targeting by surface engineering of sEVs, we focused on the selective capture of sEVs derived from MDA-MB-436 triple-negative breast cancer (TNBC) cells (cell type A in Fig. 1a) in the excessive presence of sEVs derived from MCF7 breast cancer (BC) cells and blood cells (cell types B and C, respectively, in Fig. 1a). TNBC is the most challenging subtype of BC to detect owing to its absence of the three most common types of BC cell surface receptor (ER, PR and HER2) despite its notorious recurrence and aggressive nature[24]. We targeted SA, primarily *N*-acetylneuraminic acid (Neu5Ac), a key molecule in cancer malignancy and metastasis[19–21]. The bimetallic compound TDA–Co–Eu (TCE), composed of 2,2′-thiodiacetic acid (TDA), Eu^{3+} and Co^{2+}, was utilized for its selective affinity to SA on cancer cell surfaces[25]. This unique capability arises from the competitive binding between SA and Eu^{3+} that is released from the complex. TCE was prepared by sequentially mixing solutions of TDA, Co^{2+} and Eu^{3+} (see Methods for details). Mass spectrometry revealed a mixture of compounds with varying stoichiometries of Eu^{3+}, Co^{2+} and TDA (Fig. 2a). Despite being a compound mixture, the TCE complex was effective for SA sensing, as demonstrated by the detected $(Neu5Ac)_2Eu^{3+}$ in the mass spectrum post SA reaction (Fig. 2b). Fluorometric analysis further validated the ability of SA to liberate Eu^{3+} ions from TCE, as indicated by the increased fluorescence of Eu^{3+} when binding to SA (Fig. 2c). Notably, the TCE complex displayed a pronounced (more than tenfold) affinity to SA including Neu5Ac derivatives present in both mice and humans such as Neu5Gc and Neu5Ac9Ac, compared with other biomolecules (Fig. 2d). Sialylated proteins bearing terminal SA residues, such as mucin (a highly glycosylated protein), also produced detectable signals upon mixing with the TCE complex, attributed to their SA moieties. Subsequently, sEV surfaces were modified using Eu^{3+} ions, introducing the TCE solution to sEV suspensions followed by ultracentrifugation to remove unreacted Eu^{3+} ions and residual TDA and Co^{2+}. sEVs from MDA-MB-436 cells, MCF7 cells and blood cells present in foetal bovine serum (FBS), termed sEV-MDA, sEV-MCF7 and serum-derived sEVs (sEV-BLD), respectively, underwent this Eu^{3+} ion-based surface modification (Extended Data Fig. 1). Inductively coupled plasma mass spectrometry (ICP-MS) and liquid chromatography-tandem mass spectrometry (HPLC–MS/MS) confirmed the presence of Eu^{3+} on the surface-modified sEVs, indicating that Eu^{3+} binding is the principal modification induced by the TCE treatment. The resulting surface-engineered sEVs were designated sEV-MDA-Eu, sEV-MCF7-Eu and sEV-BLD-Eu, respectively (Fig. 2e,f). These results also show the presence of SA residues on these sEVs. The increased Eu^{3+} content in sEV-MDA-Eu is probably attributed to the prominent SA expression on MDA-MB-436 cell membranes (Fig. 2g), causing sEV-MDA to possess a higher SA concentration (Fig. 2h), which then binds more Eu^{3+} from TCE. The rise in the zeta potential of these surface-engineered sEVs, compared with their unaltered counterparts, highlights the effective incorporation of Eu^{3+} (Fig. 2i).

Elevated SA levels facilitated Eu^{3+}-ion binding to host cancer cell and sEV membranes. Each Eu^{3+} ion can coordinate with more than one SA molecule, thereby enhancing sEV-mediated homotypic targeting (Fig. 1a, inset). This was demonstrated in sEV–cell culture experiments, in which Eu^{3+}-modified sEVs (sEV-MDA-Eu, sEV-MCF7-Eu and sEV-BLD-Eu), labelled with PKH67 (green), were incubated with MDA-MB-436 or MCF7 cells (Extended Data Fig. 2a). After incubation with cells, captured sEVs can either remain attached to the cell membrane or be internalized into the cytoplasm. First, we confirmed that the surface-modified sEVs exhibited minimal cytotoxicity towards host cells, as demonstrated by an MTT assay (Extended Data Fig. 2b). Laser scanning confocal microscopy (LSCM) revealed that sEV-MCF7-Eu were incorporated by MDA-MB-436 cells after 12 h, with the fluorescence intensity approaching an appreciable level at 20 h (Fig. 3a,b). By contrast, sEV-MDA-Eu achieved similar fluorescence intensity in only 6 h with MDA-MB-436 cells, indicating its quicker targeting capability (Fig. 3c). The results validated the improved sEV–cell interaction after the surface modification in comparison with sEVs without the surface modification (Fig. 3c and Extended Data Fig. 2c,d). Enhanced interactions with MCF7 cells were observed for both sEV-MDA-Eu and sEV-MCF7-Eu compared with their non-modified counterparts (Extended Data Fig. 2d,e). However, MCF7 cells exhibited a pronounced capture of sEV-MDA-Eu compared with sEV-MCF7-Eu (Extended Data Fig. 2f,g), which is presumably attributed to a denser Eu^{3+}-ion presence in the former. Furthermore, the PKH67-fluorescence tracking revealed that host MDA-MB-436 cells preferentially absorbed sEV-MDA-Eu, with substantially faster capture than other sEV types (Fig. 3c–i and Extended Data Fig. 2d,h). At the third hour, the homotypic targeting efficiency of host MDA-MB-436 cells had increased by 25.6-fold owing to the application of sEV-MDA-Eu (Fig. 3d). LSCM confirmed that sEV-MDA-Eu uniformly populated MDA-MB-436 cells after a 3-h incubation, whereas sEV-MCF7-Eu and sEV-BLD-Eu required 12 h and 40 h, respectively (Fig. 3b,c,e–h). Increasing sEV concentration reduced the capture time, demonstrating the host cells' capacity to differentiate between sEV types based on absorption rates (Fig. 3j–l). To rigorously validate the capacity of MDA-MB-436 cells for capturing sEVs derived from other MDA-MB-436 cells that simulate sEVs derived from TNBC cells, we used two-colour intracellular fluorescence imaging. sEV-MDA-Eu and sEV-MCF7-Eu were tagged separately with PKH67 (green) and DiI (red), and their interaction with MDA-MB-436 cells was monitored. By 3-h incubation, fluorescence predominantly traced sEV-MDA-Eu capture, regardless of the fluorophore used (Fig. 3m–p). After a 10-h incubation, dual fluorescence denoted the presence of both sEV types in MDA-MB-436 cells. These results further validated the elevated differential capture of Eu^{3+}-modified sEVs by host cells, depending on the sEV type.

The homotypic targeting of distinct sEVs originating from different cells and modified through surface engineering was further validated in mixed cell culture conditions. An LSCM analysis of MDA-MB-436 and MCF7 cell cocultures incubated with sEV-MDA demonstrated that sEVs from MDA-MB-436 were selectively captured by cells of the same lineage. This targeting property was maintained even after surface modification with Eu^{3+} ions (Fig. 4a). A similar trend was observed in LSCM images of cocultured cells with sEV-MCF7 (Fig. 4b). We noted the preserved and enhanced homotypic targeting of sEVs to cells following the modulation of sEVs with Eu^{3+} ions, as indicated by normalized PKH67 fluorescence intensities (Fig. 4c,d). It is worth noting that the elevated intensity of 'sEV-MDA-Eu to MCF7' compared

Fig. 2 | sEV surface modification with Eu^{3+} ions for super homotypic targeting. **a**, The mass spectrum of TCE. **b**, The mass spectrum of TCE after its reaction with SA. **c**, The fluorescence spectra of TCE for sensing different concentrations of SA (excitation wavelength, 390 nm). **d**, The fluorescence intensity differences between TCE with different linkers and the control (TCE without any linkers). Data are presented as mean ± s.d. ($n = 3$ independent samples). **e**, The ICP-MS analysis of Eu^{3+} and Co^{2+} content in different surface-engineered and intact sEVs. Data are presented as mean ± s.d. ($n = 3$ independent samples). **f**, The HPLC–MS/MS analysis of TDA content in different surface-engineered sEVs using multiple reaction monitoring mode, in which the first-stage mass spectrometry detects the TDA molecule (precursor, $m/z = 151.60$ [[TDA]H^+]) and the second-stage mass spectrometry analyses its fragment (product, $m/z = 74.05$). **g**, The flow-cytometric enumeration of BLD, MCF7 and MDA-MB-436 cells labelled with SNA-FITC, a FITC-conjugated lectin that specifically binds to SA residues. **h**, The expression levels of SA on sEVs labelled with SNA-FITC measured by a multimode microplate reader. Data are presented as mean ± s.d. ($n = 3$ independent samples). **i**, Zeta potentials of surface-engineered and intact sEVs. Data are presented as mean ± s.d. ($n = 3$ independent samples).

https://doi.org/10.1038/s41551-026-01743-2

with control groups in Fig. 4c, which was not observed in the corresponding 'sEV-MCF7-Eu to MDA' data in Fig. 4d, can be attributed to the higher SA expression on sEV-MDA than on sEV-MCF7, leading to weak non-specific binding of sEV-MDA to other cell types. Furthermore, mixed cell culture experiments demonstrated that sEVs modified with the complete TCE complex exhibited stronger homotypic specificity than those modified with Eu^{3+} ions alone (Extended Data Fig. 3a). The reduced fluorescence intensity per host cell from lanthanide-ion-only

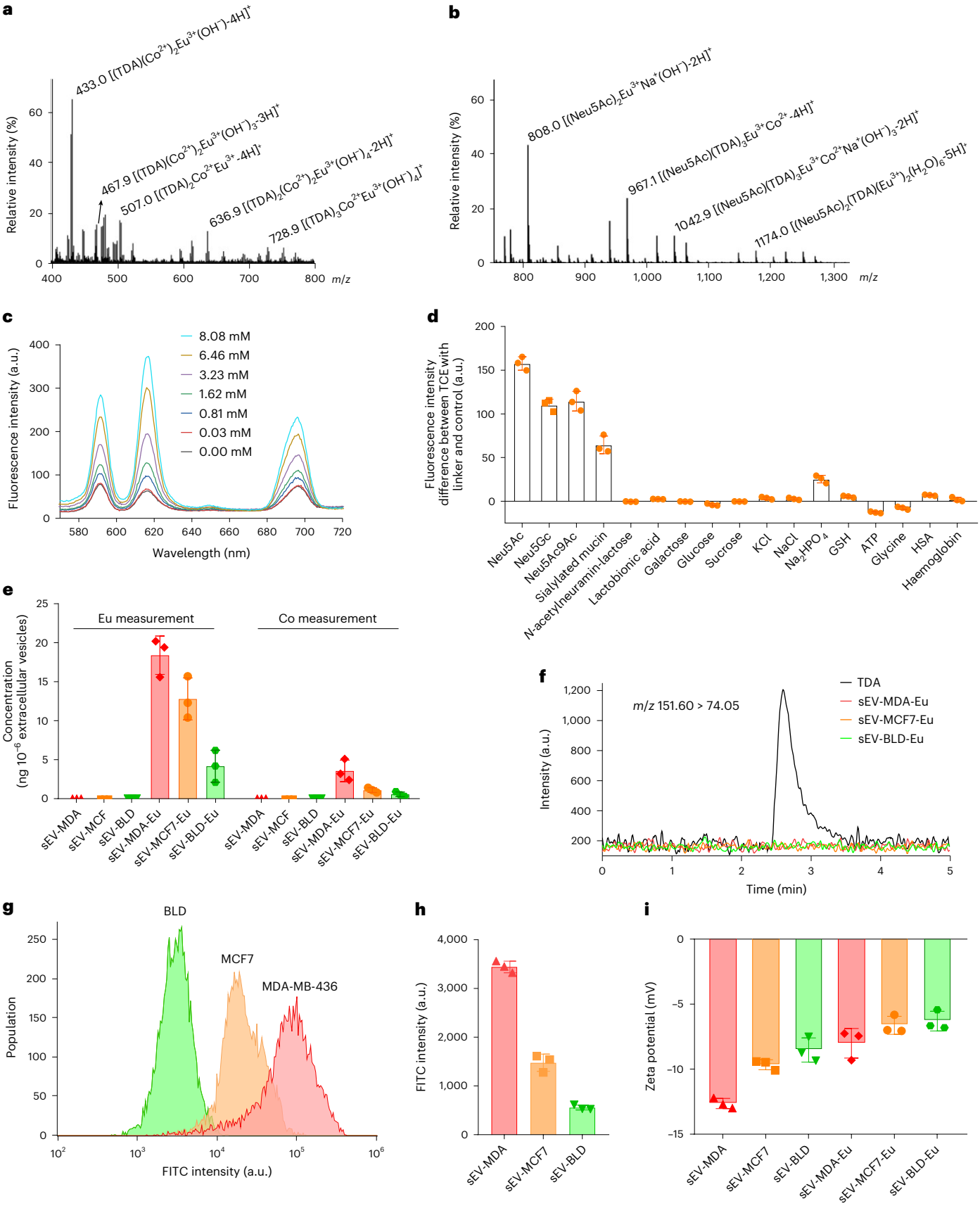

modified sEVs, compared with sEVs modified with complexes containing TDA and Co^{2+}, suggests that the bimetallic structure is essential for conferring targeting specificity (Extended Data Fig. 3b). These results highlight the role of TCE in enhancing sEV-mediated homotypic targeting efficiency, strengthening sEV–cell interactions and initiating the cell capture process without compromising selectivity of sEVs. The accumulated results underscore the preferential affinity of MDA-MB-436 cells for sEV-MDA-Eu over sEV-MCF7-Eu. Thus, MDA-MB-436 cells emerged as a selective tool for discerning between different sEV types on the basis of rapid and slow capture timelines, outpacing unmodified sEVs. This temporal differentiation offers a strategy for sEV discrimination, and the 3-h specific incubation period was chosen to maximize the specificity in detecting sEV-MDA from a mixture of sEV-MDA, sEV-MCF7 and sEV-BLD.

sEV detection based on super homotypic targeting

sEVs carry proteins, nucleic acids and lipids, reflecting the state of their origin cells, and are stable in body fluids, making them potential biomarkers for diseases such as cancer[26–30]. sEVs are an emerging marker in liquid biopsies for non-invasive cancer detection, providing insights into cancer progression and helping monitor treatment responses[31–35]. Although numerous methods have been developed to detect sEVs in blood and serum samples, their specificity falls short in differentiating tumour-specific sEVs from the overall sEV population in the sample[36,37]. Consequently, these methods tend to focus on analysing specific proteins or nucleic acids within the entire sample. The shared characteristics of proteins and nucleic acids within different sEVs complicate their analysis[38,39]. We address these problems with super homotypic targeting.

Our sEV detector based on super homotypic targeting is schematically shown in Fig. 5a. Here, we leveraged MDA-MB-436 cells as host cells to selectively capture and enrich sEVs derived from TNBC tumour cells (sEV-TNBC) in the excessive presence of other sEV populations from BC cells and blood cells (sEV-MCF7 and sEV-BLD, respectively) and subsequently analysed the enriched sEVs on the cells using flow cytometry. Specifically, a blood sample was collected from an animal subject (a mouse in this study) and subjected to differential ultracentrifugation to extract a pool of sEV-TNBC, sEV-BC and sEV-BLD. sEV-TNBC were modified with Eu^{3+} ions and fluorescently labelled with PKH67 (Extended Data Fig. 4a). During a 3-h incubation, only sEV-TNBC were captured and enriched by MDA-MB-436 cells (host cells), which were measured for accurate enumeration with a commercially available flow cytometer (CytoFLEX LX, Beckman Coulter) and a home-made imaging flow cytometer[40,41]. As mentioned above, this incubation time (3 h) was carefully chosen to optimize the specificity of detecting sEV-TNBC from the heterogeneous sEV population (Figs. 3i and 5b–e and Extended Data Fig. 4b–g).

To evaluate the sensitivity, specificity and limit of detection (LOD) of the sEV detector, we performed spike-and-recovery tests with sEV-MDA (1×10^4–1×10^7 sEVs ml^{-1}) and/or sEV-MCF7 (5×10^7 sEVs ml^{-1}) spiked into 1.0 ml of FBS (4×10^8 sEVs ml^{-1}) to mimic serum samples laden with sEV-TNBC at pathologically relevant concentrations. Flow cytometry results revealed a signal intensity boost ranging from 0.75% to 23.03%, correlating with sEV-MDA concentrations between 1.74×10^4 and 1.04×10^7 sEVs ml^{-1} (Extended Data Fig. 4d,h). These results highlight the affinity of the host cells for sEV-MDA, which persisted even in the presence of sEV-MCF7 (2.0×10^5 sEVs ml^{-1}) (Extended Data Fig. 4e–g). A compelling observation was the strong linear relationship when plotting the sEV-MDA concentration logarithmically against the count of the host cells containing sEV-MDA, indicated by a linear fit with $R^2 = 0.9011$ (Fig. 5f). On the basis of the linear fit, the LOD was estimated to be approximately $10^{2.88}$ sEVs ml^{-1} (~751 sEVs ml^{-1}) of serum containing 4×10^8 sEV-BLD, using the formula $LOD = 3.3\sigma/S$, where σ is the standard deviation of the y intercept and S is the slope of the linear fit[42]. Furthermore, Fig. 5g shows exceptional sensitivity and specificity for the detection of sEV-MDA in the serum sample (1 ml), even including sEV-MCF7 (Fig. 5h), as evidenced by the receiver operating characteristic (ROC) curve boasting an area-under-the-curve (AUC) value of 0.9300 for the selective detection of sEV-MDA in the presence of sEV-BLD and sEV-MCF7 (see Extended Data Fig. 5a,b for similar results that show the specific detection of sEV-MDA in the presence of sEV-BLD with leukaemia-derived sEVs). The imaging flow cytometry results showed a marked improvement in both sensitivity and specificity compared with the traditional flow cytometry (Fig. 5d,e and Extended Data Fig. 5c) because it effectively eliminated noisy background fluorescence signals to accurately pinpoint false positive events that arose from cell death or debris[40,43] (Extended Data Fig. 5d–f). It should be noted that the enhanced sensitivity of imaging flow cytometry may also detect a small fraction of sEV-MCF7-Eu that are non-specifically captured by MDA-MB-436 host cells, which appears as a slight increase in the gated population in Fig. 5e compared with Fig. 5d. Such effects could probably be minimized through prior signal calibration of the detection method. As a result of these enhancements, our data analysis revealed a stronger linear correlation with sEV-MDA concentration, highlighted by a notably high coefficient of determination ($R^2 = 0.9393$; Fig. 5f). In addition, we observed a tenfold boost in the estimated LOD value, settling at $10^{1.8}$ sEVs ml^{-1} (~63 sEVs ml^{-1}) of serum containing 4×10^8 sEV-BLD. The ROC curve was also pronounced, with an AUC value of 0.9796 (Fig. 5g), even including sEV-MCF7 (0.9800; Fig. 5h).

We used the fully characterized sEV detector to directly identify sEV-TNBC in serum samples from TNBC-afflicted mice (see Methods for details). First, we evaluated the sensitivity of the method using both flow cytometry and imaging flow cytometry on 1 ml serum samples isolated from blood collected 14 days after TNBC

Fig. 3 | LSCM of cancer cells incubated with surface-engineered sEVs. **a**, A schematic of mixing MDA-MB-436 cells with various surface-engineered sEVs. **b**, The LSCM-based monitoring of MDA-MB-436 cells incubated with sEV-MCF7-Eu. sEVs were labelled with PKH67 (green). Scale bar, 30 μm. **c**, The merged brightfield and fluorescence images of host MDA-MB-436 cells after incubation with sEVs from MDA-MB-436 cells (sEV-MDA-Eu) via sEV surface engineering, sEVs from MDA-MB-436 cells (sEV-MDA), sEVs from MCF7 cells (sEV-MCF7) and sEVs from blood cells (sEV-BLD) for 3, 6, 12 and 20 h. Scale bar, 30 μm. **d**, The intensity of fluorescence emitted from the captured sEVs per host MDA-MB-436 cell varied over the course of the incubation period. After a 3-h incubation, the host MDA-MB-436 cells exhibited a substantially enhanced efficiency in capturing sEV-MDA-Eu; 25.6, 834 and 2,503 times higher than with sEV-MDA, sEV-MCF7 and sEV-BLD, respectively. Data are presented as mean ± s.d. ($n = 5$ independent samples). **e**, The LSCM-based monitoring of MDA-MB-436 cells incubated with sEV-MDA-Eu for 1 h and 3 h. Scale bar, 50 μm. **f**,**g**, The fluorescence intensity values of sEV-MDA-Eu in MDA-MB-436 cells after 1-h (**f**) and 3-h (**g**) incubation. **h**, The LSCM-based monitoring of MDA-MB-436 cells incubated with sEV-BLD-Eu for 12 and 40 h. The concentration of the sEV-BLD-Eu suspension is ~3.8×10^8 sEVs ml^{-1}. Scale bar, 50 μm. **i**, The surface-engineered sEV capture for sEV-MCF7-Eu, sEV-MDA-Eu and sEV-BLD-Eu by MDA-MB-436 cells. Data are presented as mean ± s.d. ($n = 3$ independent samples). **j**–**l**, MDA-MB-436 cells incubated with 40-μl suspensions of sEV-MDA-Eu (**j**) (~4.0×10^7 sEVs ml^{-1}), sEV-MCF7-Eu (**k**) (~4.0×10^7 sEVs ml^{-1}) and sEV-BLD-Eu (**l**) (~3.8×10^8 sEVs ml^{-1}). By increasing the concentration of sEVs, MDA-MB-436 cells were able to capture sEV-MDA-Eu within 1 h, sEV-MCF7-Eu within 8 h and sEV-BLD-Eu within 30 h. Three independent experiments were performed for each case. Scale bars, 40 μm. **m**–**p**, The two-colour intracellular fluorescence imaging of host MDA-MB-436 cells incubated with sEV-MDA-Eu and sEV-MCF7-Eu for 3 h and 10 h, respectively: fluorescence intensity per cell (**m**) and representative LSCM images (**o**) of captured sEV-MDA-Eu with PKH67 labelling and captured sEV-MCF7-Eu with DiI labelling; fluorescence intensity per cell (**n**) and representative LSCM images (**p**) of captured sEV-MDA-Eu with DiI labelling and captured sEV-MCF7-Eu with PKH67 labelling. Cell nuclei were stained with DAPI (blue). In (**m**, **n**), data are presented as mean ± s.d. ($n = 100$ independent cells). Scale bars, 30 μm.

https://doi.org/10.1038/s41551-026-01743-2

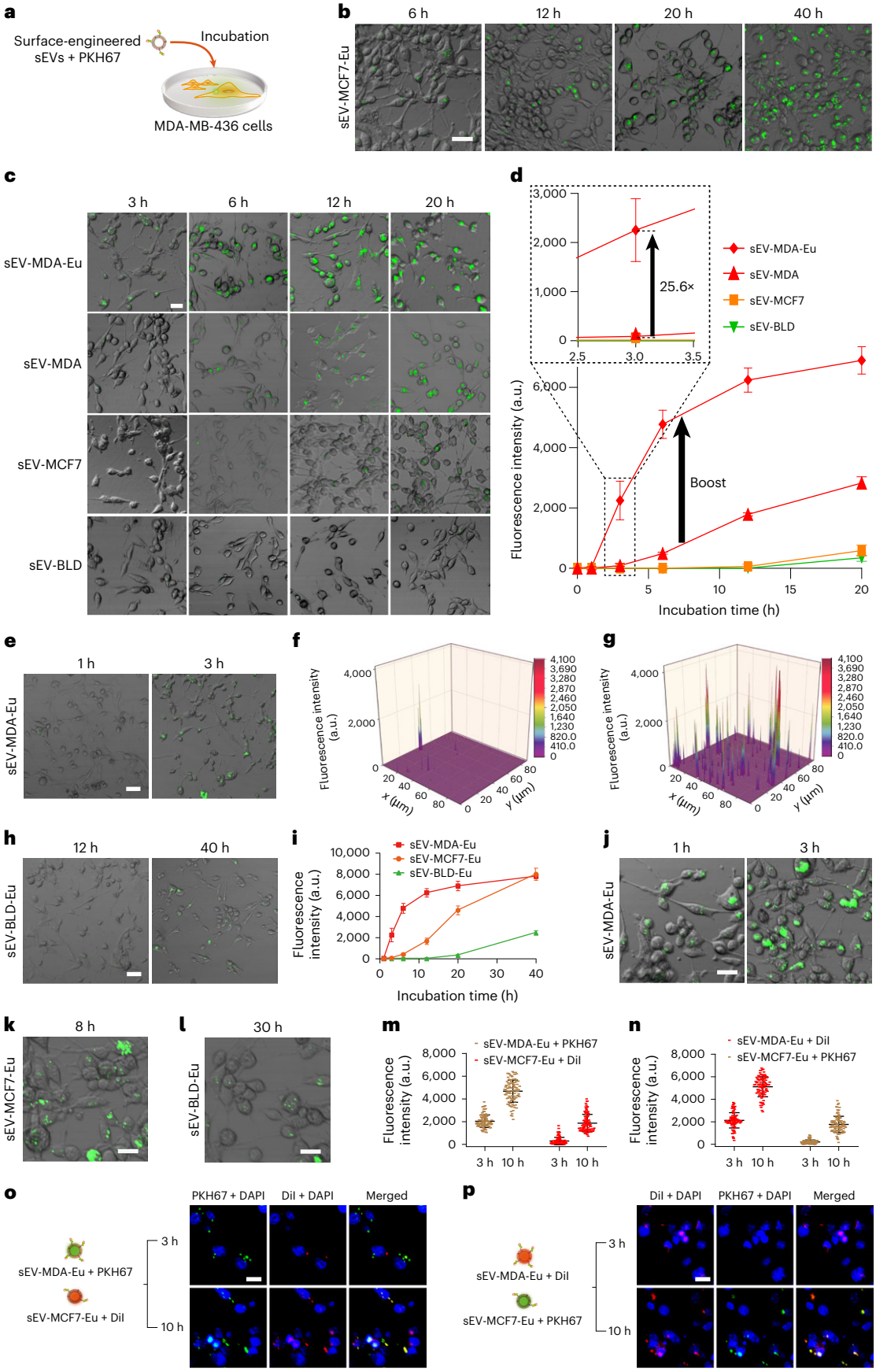

https://doi.org/10.1038/s41551-026-01743-2

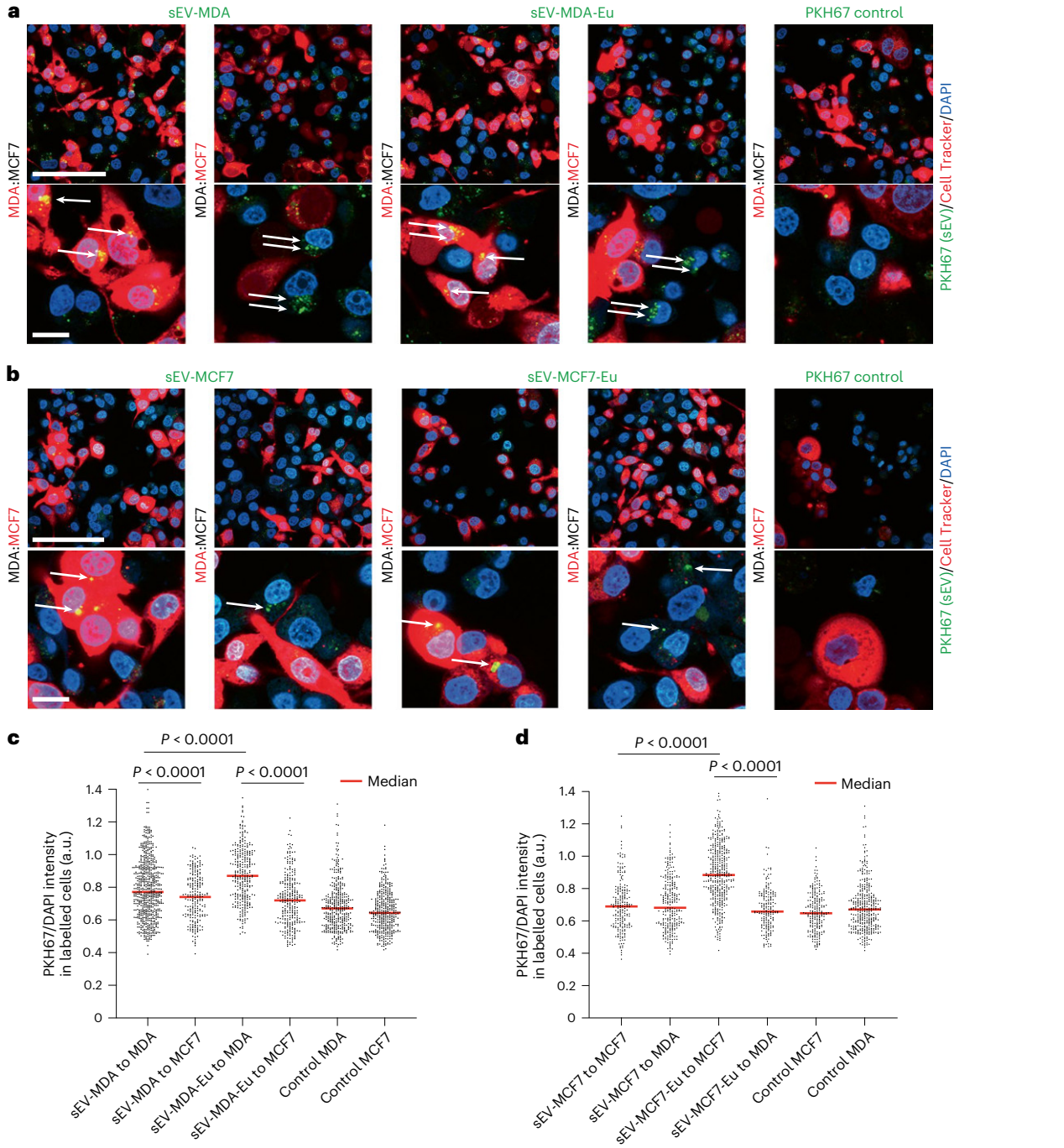

Fig. 4 | LSCM of mixed cancer cells incubated with sEVs. a, The LSCM-based monitoring of mixed cell cultures, with and without cell-tracker labelling of MDA-MB-436 and MCF7 cells, after 20-h incubation with sEV-MDA, sEV-MDA-Eu or PKH67 control. The arrows indicate sEVs captured by cells. Scale bars, 100 µm (top), 20 µm (bottom). **b**, The LSCM-based monitoring of mixed cell cultures, with and without cell-tracker labelling of MDA-MB-436 and MCF7 cells, after 20-h incubation with sEV-MCF7, sEV-MCF7-Eu or PKH67 control. The arrows indicate sEVs captured by cells. Scale bars, 100 µm (top), 20 µm (bottom). **c**,**d**, The intensity of fluorescence (PKH67/DAPI) emitted from captured sEVs, sEV-MDA or sEV-MDA-Eu ($n > 220$ cells per group) (**c**) and sEV-MCF7 or sEV-MCF7-Eu ($n > 150$ cells per group) (**d**), per labelled MDA-MB-436 or MCF7 cells. Data were analysed using one-way ANOVA with Tukey's post hoc test. Each sEV type showed a significantly higher incorporation rate in its respective homotypic cell type within the mixed cell cultures. sEVs modified with Eu^{3+} displayed a significantly higher incorporation rate than intact sEVs.

xenograft implantation. Flow cytometry effectively distinguished between the serum samples of healthy mice ($n = 5$) and those of TNBC tumour-bearing mice ($n = 5$), revealing apparent differences ($P < 0.001$) in the identification of sEV-TNBCs (Fig. 5i). When using imaging flow cytometry, as depicted in Fig. 5j, the distinction between the groups became even clearer, reflected by an even lower P value ($P < 0.0001$). These excellent P values are consistent with the aforementioned LODs and ROC curves in Fig. 5g,h. Next, to comprehensively characterize the detector performance over the course of tumour progression, we applied the detection method via flow cytometry to mouse groups sampled at multiple time points following tumour inoculation, comparing results with and without Taxol treatment[44,45]. A noticeable increase in the estimated number of sEV-TNBC was observed by day 8, probably reflecting tumour

https://doi.org/10.1038/s41551-026-01743-2

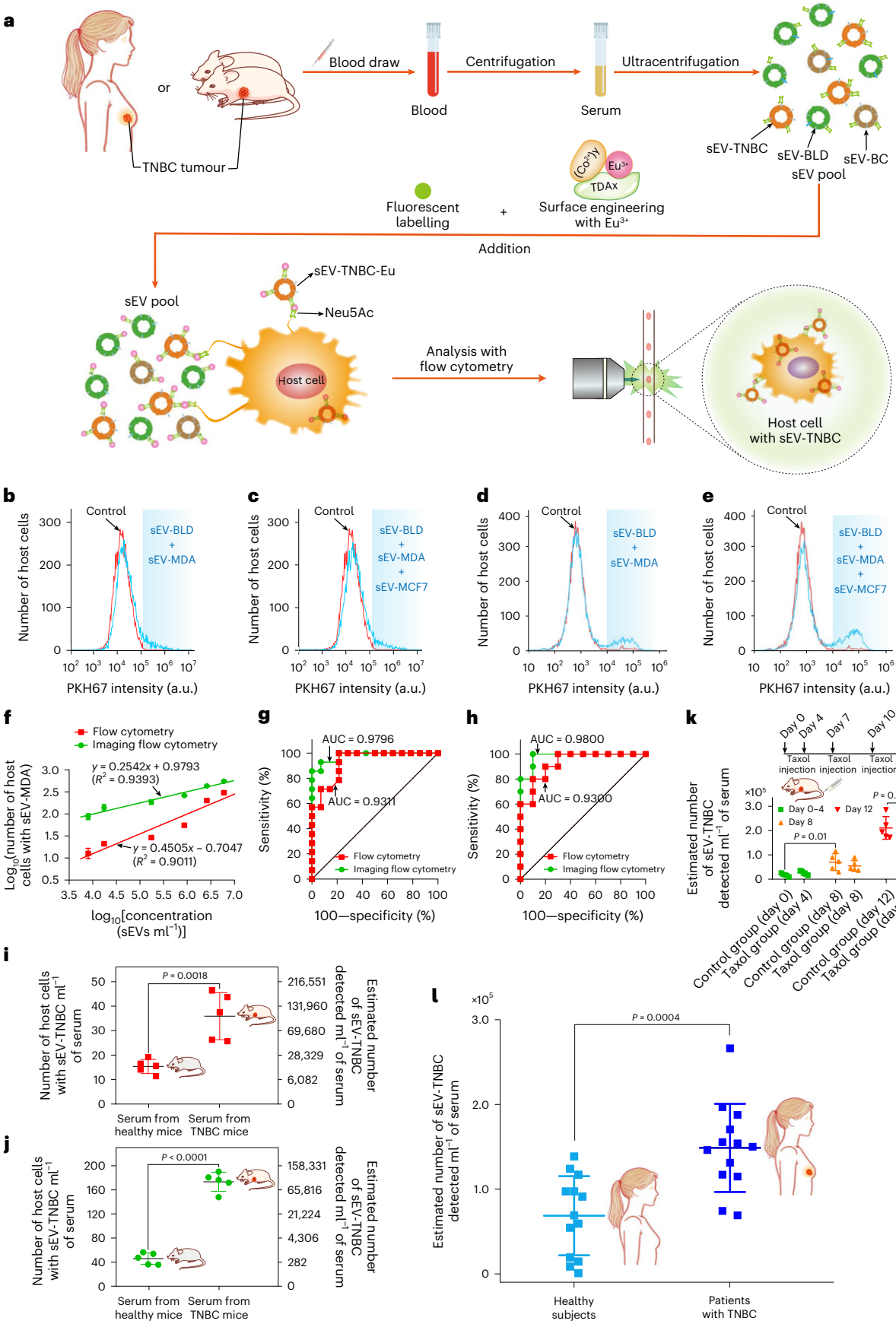

growth that promotes sEV release into circulation. By day 12, a further substantial increase in sEV levels was detected. Remarkably, Taxol-treated TNBC mice showed a significantly lower number of sEV-TNBC compared with untreated mice on day 12 ($P < 0.01$; Fig. 5k).

Finally, we used our sEV detector to identify sEV-TNBC in serum samples from patients with TNBC (see the Methods and Extended Data Tables 1 and 2 for clinical sample preparation and patient demographics). Blood was collected from clinically diagnosed patients

Fig. 5 | Schematic and demonstration of sEV detection based on super homotypic targeting. a, A schematic illustration of the sEV detection procedure based on super homotypic targeting. Blood samples are either collected from human subjects or pooled from two mice and subjected to centrifugation and ultracentrifugation to extract sEV-TNBC, sEV-BC and sEV-BLD. sEVs are modified by TCE and fluorescently labelled with PKH67. During a 3-h incubation period, only sEV-TNBC are captured and enriched by MDA-MB-436 cells (host cells), which are measured for accurate enumeration with a commercially available flow cytometer and a home-made imaging flow cytometer. **b**,**c**, The flow cytometry of host cells selectively capturing sEV-MDA in serum (1 ml) containing 2×10^5 sEV-MDA and 4×10^8 sEV-BLD without (**b**) and with (**c**) 5×10^7 sEV-MCF7, in comparison with the control (host cells without incubation with the sEVs). A total of 10,000 host cells were used for each measurement. Light blue regions indicate counting thresholds. **d**,**e**, The imaging flow cytometry of host cells selectively capturing sEV-MDA in serum (1 ml) containing 2×10^5 sEV-MDA and 4×10^8 sEV-BLD without (**d**) and with (**e**) 5×10^7 sEV-MCF7, in comparison with the control (host cells without incubation with the sEVs). A total of 10,000 host cells were used for each measurement. Light blue regions indicate counting thresholds. **f**, The number of host cells selectively capturing sEV-MDA derived from MDA-MB-436 cells at different spiked concentrations in serum (1 ml) containing about 4×10^8 sEV-BLD derived from blood cells, detected with flow cytometry and imaging flow cytometry. Data are presented as mean ± s.d. ($n = 3$ independent samples). **g**, The ROC curves for detecting sEV-MDA in the presence of sEV-BLD. **h**, The ROC curves for detecting sEV-MDA in the presence of sEV-BLD and sEV-MCF7. **i**, The number of host cells selectively capturing sEV-TNBCs in the serum of TNBC-afflicted mice, measured with flow cytometry. The result is compared with the control (healthy mice): $n = 5$ for each category. In total, 3,000 host cells were used for each measurement. An axis for the estimated number of detected sEVs based on the linear fit in **f** is also shown on the right. The *P* value was obtained using a two-sided *t*-test to assess the difference between the two groups. Data are presented as mean ± s.d. **j**, The number of host cells selectively capturing sEV-TNBC in the serum of TNBC-afflicted mice, measured with imaging flow cytometry. The result is compared with the control (healthy mice): $n = 5$ for each category. A total of 3,000 host cells were used for each measurement. An axis for the estimated number of detected sEVs based on the linear fit in **f** is also shown on the right. The *P* value was obtained using a two-sided *t*-test to assess the difference between the two groups. Data are presented as mean ± s.d. **k**, The estimated number of sEV-TNBC based on the number of host cells selectively capturing sEV-TNBC in the serum of TNBC-afflicted mice with or without Taxol treatment, measured with flow cytometry. Day 0 corresponds to tumour inoculation, whereas days 4, 7 and 10 indicate the time points of Taxol administration (20 mg kg^{-1} per injection). $n = 5$ for each group. In total, 3,000 host cells were used for each measurement. The *P* value was obtained using a two-sided *t*-test to assess the difference between groups. Data are presented as mean ± s.d. **l**, The estimated number of sEV-TNBC based on number of host cells selectively capturing sEV-TNBC in the serum of patients with TNBC, as measured by flow cytometry. The result is compared with those from healthy female control subjects: $n = 13$ for each category. The *P* value was calculated on the basis of a two-sided *t*-test to assess the difference between the two groups. Data are presented as mean ± s.d.

with TNBC, confirmed by pathological assessment showing negative expression of ER, PR and HER2, and 1 ml of serum was isolated following the same protocol used in the mouse experiments. The samples were analysed by flow cytometry and compared with serum samples from healthy subjects. As shown in Fig. 5l, the method clearly distinguished patients with TNBC ($n = 13$) from healthy subjects ($n = 13$), demonstrating obvious differences ($P < 0.001$) in the detection of sEV-TNBCs using practical clinical samples. The non-zero estimated numbers of sEVs observed in the blood of healthy subjects are probably due to minor non-specific interactions between non-TNBC sEVs and host cells. These results confirmed that the detector can robustly detect TNBC from 1 ml of serum, even under conditions reflecting real clinical complexity.

CTC detection based on super homotypic targeting

Circulating tumour cells (CTCs), which are cancer cells shed from primary tumours into the bloodstream, serve as vital indicators of the potential spread of cancer and can be early markers of metastasis, thereby aiding in the development of liquid biopsies[46–50]. Their detection is crucial for cancer diagnosis but presents challenges owing to their sparse presence among the vast, diverse populations of blood cells[51,52]. Several factors compound these difficulties: the absence of specific biomarkers for reliable CTC identification, the need for large sample volumes to capture even a single CTC or to gather statistically significant CTC populations and the phenotypic variability that CTCs exhibit, depending on their origin[53–56]. Many traditional detection methods lack the required sensitivity, specificity or both. Although conventional flow cytometry can detect CTCs, it requires time-consuming pre-enrichment steps and multiple sorting runs[53,57]. Specialized techniques that can identify CTCs are often costly and require intricate setups[53,58], limiting their widespread application. We address these limitations with super homotypic targeting.

Our CTC detector based on super homotypic targeting is schematically shown in Fig. 6a. Here, sEVs were leveraged as signal amplifiers for the ultrasensitive detection of rare CTCs with single-cell resolution in a single run of standard flow cytometry. By enhancing the homotypic

Fig. 6 | Schematic of CTC detection and validation of signal amplification of CTC-like cells based on super homotypic targeting. a, A schematic illustration of the CTC detection procedure based on super homotypic targeting. The detection procedure is as follows: (1) blood samples are collected from either human subjects or mice and subjected to centrifugation for isolating TNBC-derived CTCs, other CTCs and PBMCs; (2) the surface of sEVs derived from cells of the MDA-MB-436 TNBC cell line is engineered with Tb^{3+} ions, after loading the sEVs with HAL; (3) the HAL-loaded surface-engineered sEVs are added to the blood sample and incubated with it so that they can specifically bind to the TNBC-derived CTCs; (4) after removing uncaptured sEVs, all CTCs and PBMCs are completely disrupted by ultrasonication, resulting in the release of HAL; (5) the released HAL is incubated with reporter cells (MDA-MB-436 cells) to convert HAL into PpIX within the cells; and (6) the reporter cells are analysed with a flow cytometer to count the fluorescent population of the reporter cells. **b**, A schematic of staining MDA-MB-436 cells (reporter cells) with HAL released by ultrasonicated CTC-like cells to turn them into reporter cells. **c**, LSCM images and fluorescence intensities of reporter cells after incubation with ultrasonicated PBMCs with 30 spiked CTC-like cells for varying incubation durations (1–3 h). The PBMCs with CTC-like cells were pre-incubated with HAL-loaded sEV-MDA-Tb (1.6×10^6 sEVs ml^{-1}) in a culture medium with 0.8 μg ml^{-1} TCT for 1 h. Scale bar, 20 μm. **d**, The fluorescence intensity of suspended reporter cells after incubation with ultrasonicated PBMCs with 30 spiked CTC-like cells for varying incubation durations (0.5–4 h). Data are presented as mean ± s.d. ($n = 3$ independent samples). The fluorescence intensity values shown in the figure were obtained by calculating the total fluorescence intensity from each cell and dividing it by the total number of cells ($n = 30–50$). **e**, The fluorescence intensity of suspended reporter cells after 3-h incubation with ultrasonicated PBMCs with varying spiked CTC-like cell numbers (1–30 cells). Data are presented as mean ± s.d. ($n = 3$ independent samples). The fluorescence intensity values shown in the figure were obtained by calculating the total fluorescence intensity from each cell and dividing it by the total number of cells ($n = 30–50$). **f**, LSCM images and fluorescence intensities of reporter cells after incubation with ultrasonicated PBMCs with a single spiked CTC-like cell for varying incubation durations (1–3 h). Scale bars, 20 μm. **g**, The HAL concentration in each sEV measured by HPLC across various loading durations, ranging from 20 to 120 min. sEV-MDA-Tb were incubated with 0.5 mM HAL. Data are presented as mean ± s.d. ($n = 3$ independent samples). **h**, The influence of the HAL concentration on flow cytometry of reporter cells. sEV-MDA-Tb was incubated with varying HAL concentrations (0.05–1.00 mM) for 1 h before incubation with 30 CTC-like cells and HAL introduction to reporter cells. **i**, The influence of the HAL incubation duration on flow cytometry of reporter cells. sEV-MDA-Tb was incubated with 0.5 mM HAL for varying incubation durations (10–90 min) before incubation with 30 CTC-like cells and HAL introduction to reporter cells.

https://doi.org/10.1038/s41551-026-01743-2

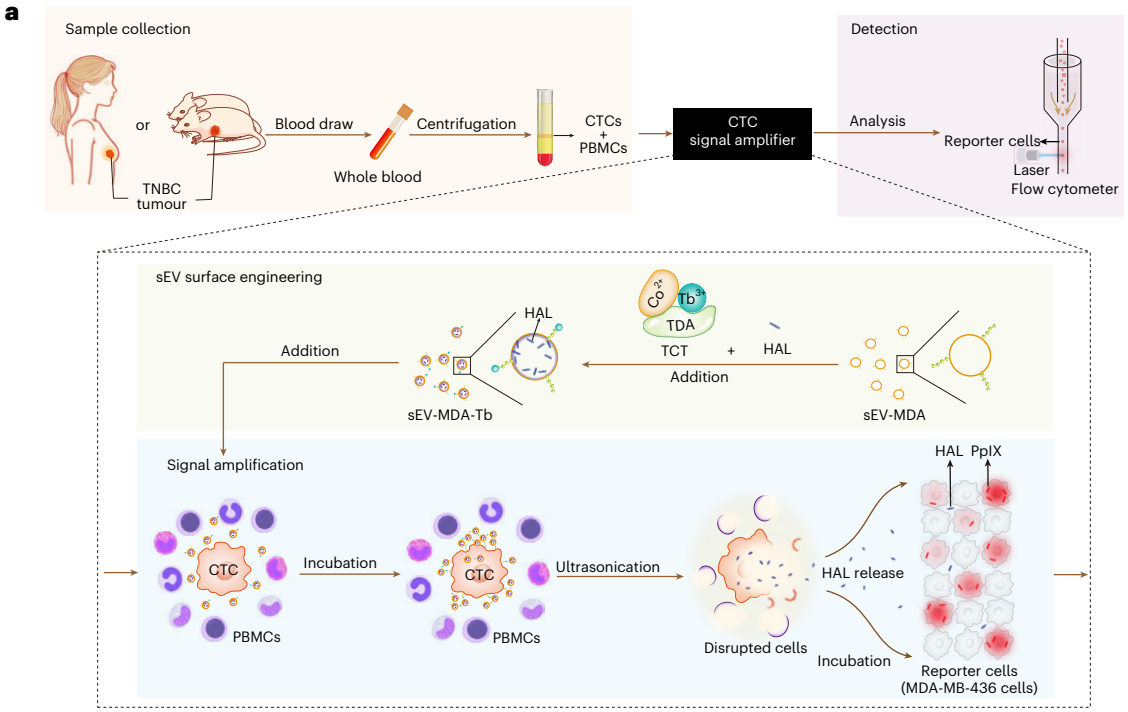

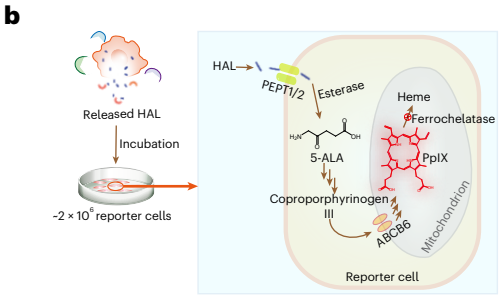

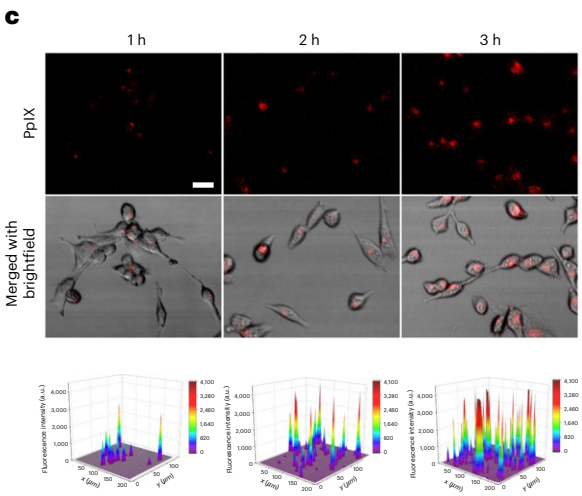

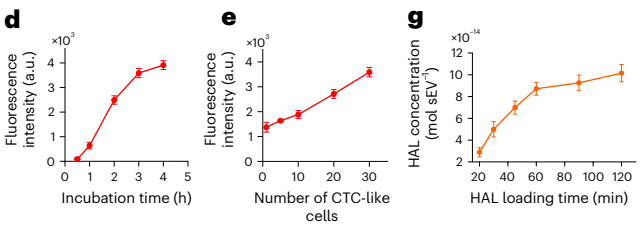

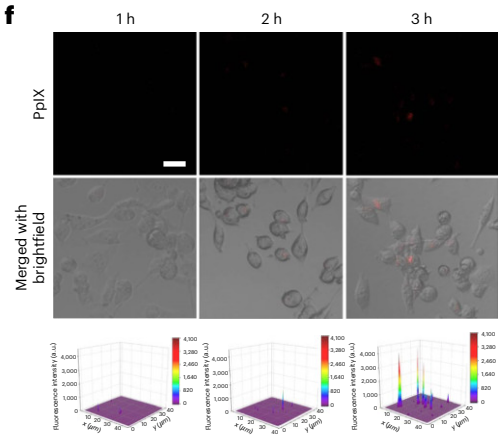

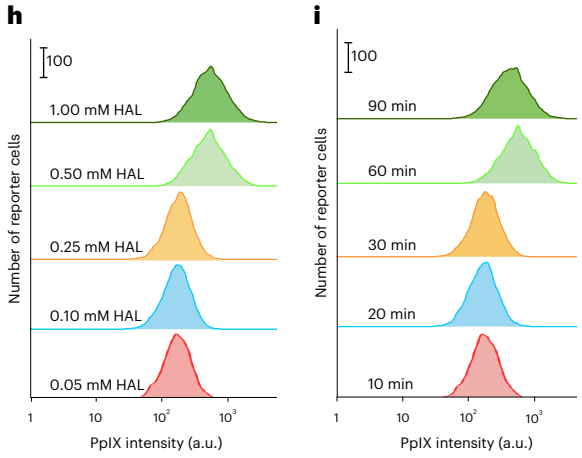

https://doi.org/10.1038/s41551-026-01743-2

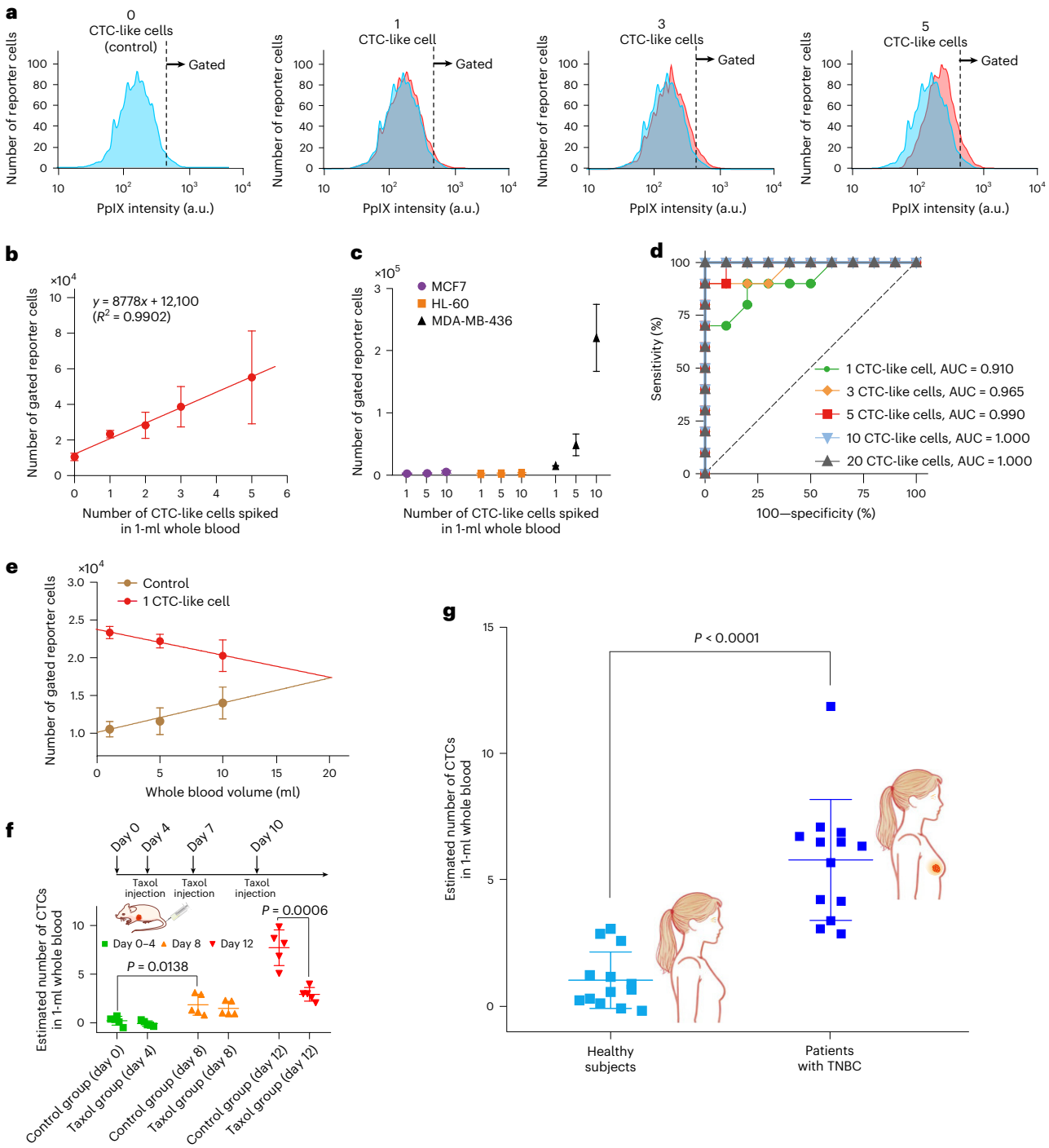

Fig. 7 | Demonstration of CTC detection based on super homotypic targeting. **a**, The flow cytometry of reporter cells amplifying signals from varying numbers of CTC-like cells spiked in 1-ml mouse whole blood as shown in light red, in comparison with the control as shown in light blue (no CTC-like cells present). Each measurement used 2×10^6 reporter cells. Dotted lines indicate gating thresholds for reporter cells. **b**, The number of gated reporter cells relative to different numbers of CTC-like cells spiked in 1-ml whole blood samples. Data are presented as mean ± s.d. ($n = 3$ independent samples). **c**, The number of gated reporter cells based on different CTC-like cells (MCF7, HL-60 and MDA-MB-436) spiked in 1-ml whole blood with varying numbers of spiked cells. Data are presented as mean ± s.d. ($n = 3$ independent samples). **d**, The ROC curves for detecting different numbers of CTC-like cells in 1-ml whole blood samples. **e**, The detection of a single CTC-like cell across varied whole blood sample volumes. The number of the gated reporter cells in the control (that is, background noise) intersects with that from the whole blood sample containing a single CTC-like cell at approximately 18.9 ml. Data are presented as mean ± s.d. ($n = 3$ independent samples). **f**, The estimated number of CTCs based on the number of gated reporter cells (MDA-MB-436) in whole blood of TNBC-afflicted mice with or without Taxol treatment, measured with flow cytometry. Day 0 corresponds to tumour inoculation, whereas days 4, 7 and 10 indicate the time points of Taxol administration (20 mg kg^{-1} per injection). $n = 5$ for each group. Each measurement used 1-ml whole blood and 2×10^6 reporter cells. The P value was obtained using a two-sided t-test to assess the difference between groups. Data are presented as mean ± s.d. **g**, The estimated number of CTCs based on the number of gated reporter cells in 1-ml whole blood of patients with TNBC, as measured by flow cytometry. The result is compared with those from healthy female control subjects: $n = 13$ for each category. The P value calculated on the basis of a two-sided t-test to assess the difference between the two groups. Data are presented as mean ± s.d.

targeting capabilities of CTCs via surface engineering of sEV-MDA, this method used probes specifically directed to TNBC cells and produced fluorescence from approximately 10,000 MDA-MB-436 cells (reporter cells) for each CTC, effectively boosting the flow cytometer's ability to detect them. Essentially, this method magnified the apparent number of rare CTCs by about four orders of magnitude, echoing the function of operational amplifiers in electronics. Specifically, a blood sample was collected from an animal subject (a mouse in this study) with TNBC and subjected to centrifugation for isolating TNBC-derived CTCs, CTCs derived from other cancer types and peripheral blood mononuclear cells (PBMCs). The surface of sEV-MDA was modified with Tb^{3+} ions released from the metal complex TDA–Co–Tb (TCT) comprising TDA, Co^{2+} and Tb^{3+} ions[25], using a procedure similar to the established protocol used for the Eu^{3+} ion surface modification (see the Supplementary Information for details), after loading the sEVs (sEV-MDA) with hexaminolevulinate (HAL)[55,59,60]. The HAL-loaded surface-engineered sEVs were added to the blood sample and incubated with it such that they could specifically bind to the CTCs. After removing uncaptured sEVs, all CTCs and PBMCs were completely disrupted by ultrasonication, resulting in the release of HAL. The released HAL was incubated with 2×10^6 reporter cells to convert HAL into the fluorescent compound, protoporphyrin IX (PpIX), within the cells, where PpIX produced strong fluorescence in mitochondria owing to their reduced metabolism in converting PpIX to haem[60] (Fig. 6b). The reporter cells were analysed with a commercially available flow cytometer operating in single-colour mode (CytoFLEX LX, Beckman Coulter) to count the fluorescent population of the reporter cells in a single measurement run. The reason why we selected Tb^{3+} ions over Eu^{3+} ions was to avoid fluorescence overlap between PpIX and Eu^{3+} ions.

In our approach to detect CTCs using standard flow cytometry, we utilized MDA-MB-436 cells as a model for CTCs derived from TNBC tumours, labelling them with HAL[55,59,60]. Typically, the low concentration of PpIX in sparse CTCs results in insufficient signals for flow cytometry. However, we substantially boosted the signal by using sEV-mediated homotypic targeting, further enhanced by modifying sEV surfaces with Tb^{3+} ions. HAL-loaded and Tb^{3+} ion-enhanced sEV-MDA effectively targeted CTC-like MDA-MB-436 cells, even in the presence of a high concentration of PBMCs. During this process, HAL was primarily contained within the sEV-MDA-Tb, preventing PpIX formation in the MDA-MB-436 cells. After centrifugation to remove unbound sEV-MDA-Tb, the cells were ultrasonicated to disrupt them completely. The contents released from these disrupted cells, including HAL, were then introduced into a pool of about 2×10^6 MDA-MB-436 reporter cells (Fig. 6a,b). Here, HAL entered the cells through the PEPT1/2 channel and converted to PpIX, accumulating in their mitochondria (Fig. 6c–f). A 3-h incubation produced PpIX signals in roughly 1×10^4 reporter cells for each CTC-like cell, substantially enhancing flow-cytometric detection against a background noise level of approximately 1×10^4 reporter cells (Extended Data Fig. 6a–c). Notably, incubating 0.5 mM HAL with sEV-MDA for just 1 h before their surface modification and capture by CTC-like cells resulted in efficient HAL loading into the sEVs and a substantial amplification of the final signal (Fig. 6g–i).

To evaluate the sensitivity, specificity and LOD of the high-precision CTC detector, we conducted the ultrasensitive detection and enumeration of CTC-like cells in whole mouse blood using cost-effective, single-colour mode flow cytometry (see Methods for details). Initially, we assessed sensitivity by counting CTC-like cells added to 1 ml of PBS. When HAL was released from an sEV-MDA-Tb treated CTC-like cell into 2×10^6 reporter cells, about 0.75% (or 1.5×10^4 cells) exhibited an increased PpIX signal compared with the control without CTC-like cells (Extended Data Fig. 6b,c). A clear linear relationship emerged between the number of CTC-like cells and the rise in gated PpIX-positive reporter cells (Extended Data Fig. 6c, inset). However, beyond five CTC-like cells, a nonlinear increase in reporter cell count occurred owing to excessive HAL-loaded sEV-MDA in each cell, leading to saturation. We then introduced CTC-like cells into 1 ml of whole mouse blood to mimic samples with rare CTCs (Extended Data Fig. 6d). Flow cytometry showed outstanding detection capabilities, with signal intensity increases from 0.59% to 36.1% correlating with 1–20 spiked CTC-like cells in the blood (Fig. 7a,b and Extended Data Fig. 6e,f). Approximately 0.75% of reporter cells, which was equivalent to 1.5×10^4 cells, showed a heightened PpIX signal compared with the control sample, which contained no CTC-like cells. This difference defined the baseline noise level for measuring the CTC signal (Fig. 7b). We verified a robust linear correlation when charting the number of CTC-like cells against the count of gated PpIX-labelled reporter cells, reflected by a linear fit with an R^2 value of 0.9902 (Fig. 7b). Notably, when the steps of cell disruption and HAL introduction to reporter cells were omitted, no increase in signal intensity was observed for samples containing fewer than 50 CTC-like cells, indicating that these steps are essential for achieving the signal amplification required to detect rare CTC-like cells in blood (Extended Data Fig. 7). Recognizing the potential development of secondary acute myeloid leukaemia during TNBC treatment[61,62], we evaluated both the acute myeloid leukaemia cell line, HL-60, and the non-TNBC BC cell line, MCF7. The outcomes indicated elevated specificity, with a negligible signal observed for sEVs from both HL-60 and MCF7 cells (Fig. 7c). Figure 7d emphasizes the unparalleled sensitivity and specificity of this method in recognizing CTC-like cells in a 1-ml whole blood sample, corroborated by ROC curves with impressive AUC values of 0.910, 0.965 and 0.990 for 1, 3 and 5 CTC-like cells, respectively. Furthermore, to determine the LOD, we examined 5-ml and 10-ml whole blood samples in addition to the 1-ml whole blood samples and consistently observed sensitive detection, discerning signals tied to a single CTC-like cell (Fig. 7e). The declining sensitivity trend is probably attributed to the increasing number of PBMCs, which may impede the efficient interaction between sEVs from CTC-like cells and reporter cells. Using the linear fit as our guide, we calculated the maximal volume of whole blood where the signal of a single CTC-like cell was equivalent to the background noise (that is, control) as about 19 ml. These data suggest that our CTC detector is adept at amplifying signals, enabling the specific identification of just one CTC-like cell within over 10 ml of whole blood, amid roughly 10^{11} erythrocytes and 10^8 leucocytes.

We used the fully evaluated CTC detector to directly detect CTCs originating from TNBC tumours in whole blood samples procured from TNBC-afflicted mice with and without Taxol treatment (Fig. 7f, Methods). Peripheral blood samples of 1 ml each were drawn on day 4, 8 and 12 subsequent to the initiation of the TNBC xenograft in mice. After the aforementioned preparation and CTC signal amplification steps, the samples were analysed with the flow cytometer. The derived results revealed that a single run of flow cytometry, even with the affordable flow cytometer operating in single-colour mode, was sufficient to detect a clear difference between the whole blood samples collected at day 0 ($n = 5$) and those collected at day 8 ($n = 5$), on the basis of the estimated count of CTCs derived from the linear fit in Fig. 7b with saturation-induced nonlinearity corrections (Extended Data Fig. 6f). By day 12, five to ten CTCs originating from TNBC tumours were detected in the blood of untreated mice, whereas samples from Taxol-treated mice exhibited a markedly lower estimated CTC count. This difference was statistically significant, with a P value < 0.001.

Finally, we validated our CTC detector in a practical clinical setting using blood samples from patients with TNBC. Specifically, CTCs were detected in human whole blood samples to distinguish patients with TNBC from healthy subjects. For this validation, 1 ml of whole blood was collected from each of 13 clinically diagnosed patients with TNBC, confirmed by pathological assessment showing negative expression of ER, PR and HER2 (see Methods and Extended Data Tables 1 and 2 for clinical sample preparation and patient demographics). CTC signals were amplified using the same detection and processing steps described above. The samples were then analysed by flow cytometry and compared with those prepared from 13 healthy control samples.

The CTC detector exhibited a clear difference between patient and control groups ($P < 0.0001$; Fig. 7g), confirming its strong capability for sensitive detection of CTCs even under the complex biological conditions of human blood. The non-zero estimated CTC counts observed in the blood of healthy subjects are probably attributable to minor non-specific interactions between TNBC sEVs and PBMCs.

Discussion

In this study, we developed a method for super homotypic targeting by engineering the surface of sEVs with lanthanide ions, demonstrating its efficacy in precision detectors with exceptional performance. This super homotypic targeting markedly enhanced cell–sEV interactions between cells and sEVs of the same lineage by more than 25-fold compared with unmodified controls. Leveraging this phenomenon, we established two high-sensitivity liquid biopsy approaches: sEV detection, in which host cells efficiently captured lanthanide-engineered serum sEVs derived from TNBC, enabling the detection of as few as tens to hundreds of sEV-TNBCs per millilitre within highly heterogeneous sEV populations; and CTC detection, in which surface-engineered sEVs functioned as probes for high-specificity recognition and signal amplification of TNBC-derived CTCs in blood, achieving single-cell level detection sensitivity. Overall, the super homotypic targeting strategy establishes a versatile and ultrasensitive analytical framework for liquid biopsy, offering strong potential for future clinical applications.

However, certain challenges persist. The sEV and CTC detectors based on super homotypic targeting still face certain limitations, such as their multistep operational workflow and dependence on specialized instrumentation. In particular, in the CTC detection, the current approach does not permit direct downstream molecular or phenotypic analysis of captured CTCs, as the signal amplification process involves cell disruption to achieve the ultra-high sensitivity required for detecting rare individual CTCs. To further enhance the functional and translational value of this technology, future developments should aim to simplify the workflow and integrate super homotypic targeting with advanced analytical techniques such as single-cell or single-sEV transcriptomics, proteomics and other omics-based profiling methods[63].

Beyond the cancer detection context explored in this study, the scope of super homotypic targeting extends broadly across various biological and medical fields. In clinical diagnostics, this strategy holds particular promise for minimal residual disease assessment in patients with cancer, enabling a more accurate monitoring of treatment efficacy, early relapse prediction and personalized therapeutic decision-making. In cancer therapy[5,11,14], it could enable the precise targeting of tumour cells, minimizing damage to healthy tissue, which in turn will improve treatment outcomes and lessen adverse effects. In tissue engineering[15,16], it may foster more effective tissue regeneration and repair by promoting the growth and organization of specific cell types, for example in healing wounds or replacing damaged organs. It may also enhance the rejuvenating effects introduced to aged cells and organs through exposure to young sEVs[64,65]. This approach could also advance stem cell therapies by guiding stem cells to particular tissues or organs, thus improving their integration and effectiveness. A better understanding of homotypic interactions is expected to enhance our understanding of cellular communication, aiding in more accurate disease modelling and drug development. In immunotherapy[66], it may enhance the targeting of immune cells, bolstering the body's natural defences against diseases. Moreover, this method has potential in combating drug resistance, a substantial challenge in treating chronic infections and cancer, by enabling drug-loaded sEVs to achieve high intracellular drug accumulation in target cells and thereby overcome efflux-mediated and dose-limited resistance mechanisms[67]. Finally, super homotypic targeting aligns with the principles of personalized medicine, potentially enabling the more precise tailoring of treatments to individual patient profiles.

Methods

Chemicals and reagents

HAL hydrochloride (98%), $Eu(NO_3)_3{\cdot}6H_2O$ (≥99%), $TbCl_3{\cdot}6H_2O$ (≥99%), 4′,6-diamidino-2-phenylindole dihydrochloride (DAPI) (≥95%), human serum albumin (≥96%), R6G (≥95%), Neu5Ac (≥98%), GSH (≥99%), proline (99%), L-histidine (≥99%), lysine (98%), glycine (≥99%), ATP (≥98%), glucose (98%), mucin, haemoglobin, DiI, PKH67 and Green Fluorescent Cell Linker Kit were purchased from Aladdin Reagent and Sigma-Aldrich. $Co(NO_3)_2{\cdot}6H_2O$ and TDA (≥98%) were purchased from Aladdin Reagent and Fujifilm Wako Pure Chemical Corporation, respectively. Neu5Gc, Neu5Ac9Ac, *N*-acetylneuramin-lactose, lactobionic acid, sucrose and galactose were purchased from Macklin. Other chemicals and reagents were obtained from commercial suppliers and used without further purification: Roswell Park Memorial Institute (RPMI)-1640 medium and Dulbecco's modified Eagle medium (DMEM) basic (1×) (Gibco), penicillin–streptomycin (PS; Beyotime), sEV-depleted FBS, Sambucus Nigra (Elderberry Bark) Lectin (SNA, EBL), fluorescein (FITC; Thermo Fisher).

Instrumentation

Fluorescence spectra of TCT and TCE for SA sensing were obtained using a Shimadzu RF-6000 instrument. sEV isolation was facilitated by an L-70 Ultracentrifuge from Beckman Optima. Morphological characterizations of the sEVs were conducted using a JEM-1400Flash TEM system. The Zetasizer Nano ZS90 instrument from Malvern Panalytical was utilized to determine sizes and zeta potentials. Olympus's LSCM system (FV1200) was used for cell imaging. ICP-MS readings were taken with an Agilent 7500 instrument. HPLC–MS/MS analysis was obtained using a Shimadzu LCMS-8040 instrument. sEV concentrations were measured using a ZetaView NTA PMX-120 device. Flow-cytometric analyses of cells were executed using the CytoFLEX LX from Beckman Coulter.

Cell culture

MCF7 (ATCC, HTB-22), MDA-MB-436 (ATCC, HTB-130) and HepG2 (ATCC, HB-8065) cells were separately cultured in high-glucose DMEM supplemented with 1% PS and 10% FBS. K562 cells (ATCC, CCL-243) were cultured in RPMI-1640 medium supplemented with 1% PS and 10% FBS. HL-60 (ATCC, CCL-240) cells were cultured in RPMI-1640 medium supplemented with 1% PS and 13% FBS. All cell lines were incubated at 37 °C in a humidified atmosphere (approximately 95% relative humidity) containing 5% CO_2.

sEV isolation

MDA-MB-436 and MCF7 cells were cultivated separately in DMEM supplemented with 1% PS and 10% sEV-depleted FBS for 48 h, whereas K562 cells were grown in RPMI-1640 medium with the same supplements. Conditioned media from MDA-MB-436 and MCF7 cells (~ 70% confluence) were collected and subjected to differential centrifugation with 50 ml total volume[68]: 300*g* for 10 min, 2,000*g* for 10 min, 10,000*g* for 30 min and ultracentrifugation at 100,000*g* for 80 min. The resulting pellets were resuspended in 500 µl 1× PBS and stored at −80 °C as sEV-MDA and sEV-MCF7. For sEV-BLD, FBS or serum from tumour-bearing mice (1.0 ml) was blended with 1.0 ml 1× PBS and processed using the same centrifugation protocol. The resulting sEV-BLD was resuspended in 1.0 ml 1× PBS and kept at −80 °C. sEVs were characterized by transmission electron microscopy (TEM), western blotting, nanoparticle tracking analysis and dynamic light scattering to confirm the reproducibility of the isolation and modification protocols (Extended Data Fig. 1a–e).

Analysis of sEVs with western blotting

sEV-MDA, sEV-MCF7 and sEV-BLD were diluted to a concentration of approximately 4.0×10^7 sEVs ml^{-1}. Proteins were extracted from the sEVs using radioimmunoprecipitation buffer, supplemented with 1% protease

and phosphatase inhibitor cocktail on ice. These proteins were then fractionated using SDS–polyacrylamide gel electrophoresis and electro-transferred to nitrocellulose membranes. After blocking with 5% non-fat milk, the nitrocellulose membranes were probed overnight at 4 °C with primary antibodies against TSG101, CD63 and Alix: Rabbit anti-TSG101 (Abcam, ab125011, Clone EPR7130(B), 1:1,000), Rabbit anti-CD63 (Cell Signaling Technology, 52090, Clone E1W3T, 1:1,000), Rabbit anti-Alix (Abcam, ab186429, Clone EPR15314, 1:1,000). This was followed by a 2-h incubation with the horseradish peroxidase (HRP)-linked secondary antibodies (anti-rabbit IgG, HRP linked, Cell Signaling Technology, 7074, 1:5,000) at ambient temperature. Protein bands were finally visualized with enhanced chemiluminescence reagent.

Preparation of TCE

TDA (0.60 g) and $Co(NO_3)_2{\cdot}6H_2O$ (0.89 g) were dissolved in 5.0 ml H_2O and gently shaken for 0.5 h. Then, 0.59 g $Eu(NO_3)_3{\cdot}6H_2O$ dissolved in 5.0 ml H_2O was added. The mixture was gently shaken for 1 h. The resulting TCE solution (0.16 g ml^{-1}) was stored at 4 °C.

Preparation of TCT

TDA (0.69 g) and $Co(NO_3)_2{\cdot}6H_2O$ (0.89 g) were dissolved in 5.0 ml H_2O and gently shaken for 1 h. Then, 0.43 g $TbCl_3{\cdot}6H_2O$ dissolved in 5.0 ml H_2O was added. The mixture was gently shaken for 1 h. The resulting TCT solution (0.16 g ml^{-1}) was stored at 4 °C.

Detection of SA with TCE

Various concentrations of SA solution in water ranging from 0.032 mM to 8.08 mM (200 µl each), were combined with 200 µl of TCE solution (7.0 mg ml^{-1}) in water. Following a 5-min incubation, the fluorescence intensity of Eu^{3+} was recorded by a fluorescence spectrophotometer (RF-6000, Shimadzu). To evaluate the selectivity of SA detection, we examined potential interfering substances such as Na^+, HPO_4^{2-}, K^+, glucose, GSH, glycine, HSA and ATP. The conditions applied for SA detection were mirrored for this selectivity testing.

Detection of SA with TCT

Various concentrations of SA solution in water, ranging from 0.5 mM to 10 mM (200 µl each), were combined with 200 µl of TCT solution (5.0 mg ml^{-1}) in water. Following a 5-min incubation, the fluorescence intensity of Tb^{3+} was recorded with a fluorescence spectrophotometer (RF-6000, Shimadzu). To evaluate the selectivity of SA detection, we examined potentially interfering substances such as lysine, proline, glycine, cysteine, L-histidine, GSH and glucose. The conditions applied for SA detection were mirrored for this selectivity assessment.

Engineering sEV surfaces with TCE

sEV-MDA, sEV-MCF7 and sEV-BLD were resuspended in 500 µl 1× PBS (~4.0×10^7 sEVs ml^{-1}) and stained with PKH67 by mixing with 10 µl diluent containing 0.8 µl PKH67 (MIDI67 -1KT) for 1 min. Excess dye was removed with 10% sEV-depleted FBS, followed by centrifugation at 100,000*g* for 80 min and resuspension in 500 µl 1× PBS. For Eu^{3+} surface modification, sEVs were resuspended in 500 µl 1× PBS and stained with PKH67 or DiI (10 µM) as described above. After quenching with 10% sEV-depleted FBS, 8.0 µl TCE solution was added and the mixture was agitated for 1 min, followed by centrifugation at 100,000 *g* for 80 min. The resulting sEV-MDA-Eu, sEV-MCF7-Eu and sEV-BLD-Eu were resuspended in 500 µl 1× PBS. Engineered sEVs were stored at 4 °C for up to 1 week or at −80 °C for long-term storage.

Engineering sEV surfaces with TCT

sEV-MDA and sEV-MCF7 were resuspended in 500 µl 1× PBS (~4.0×10^7 sEVs ml^{-1}), stained with PKH67 as described above, washed with 10% sEV-depleted FBS and incubated with 8.0 µl TCT solution (0.1 g ml^{-1}) for 1 min. Samples were centrifuged at 100,000*g* for 80 min and resuspended in 500 µl 1× PBS to obtain sEV-MDA-Tb and sEV-MCF7-Tb. Engineered sEVs were stored at 4 °C for up to 1 week or at −80 °C for long-term storage. For HAL-labelled sEVs, sEV-MDA (~4.0×10^7 sEVs ml^{-1} in 500 µl 1× PBS) were incubated with 100 µl HAL (0.5 mM) for 1 h, followed by addition of 8.0 µl TCT solution (0.1 g ml^{-1}), agitation for 1 min and centrifugation at 100,000*g* for 80 min. The resulting HAL-loaded sEV-MDA-Tb were resuspended in 500 µl 1× PBS. HAL loading was quantified by HPLC (LC-20AT, Shimadzu) with UV detection at 210 nm using a C8 column (250 mm× 4.6 mm, 5 µm).

LSCM of sEV capture by cancer cells

MDA-MB-436 or MCF7 cells were seeded in glass-bottom confocal dishes (3 cm in diameter) with 2 ml culture medium. Approximately 5×10^5 cells were treated with 20–40 µl of various sEV suspensions: sEV-MDA, sEV-MCF7, sEV-BLD, sEV-MDA-Eu, sEV-MCF7-Eu or sEV-BLD-Eu. The concentrations of sEV-MDA, sEV-MCF7, sEV-MDA-Eu and sEV-MCF7-Eu were approximately 4.0×10^7 sEVs ml^{-1}, whereas sEV-BLD and sEV-BLD-Eu were at about 3.8×10^8 sEVs ml^{-1}. Cells were incubated with the sEVs for varying durations between 1 h and 40 h. After incubation, cells were rinsed with 1× PBS before undergoing LSCM analysis.

LSCM of sEV capture in the mixed cell culture experiment

To label cells, MDA-MB-436 or MCF7 cells were incubated with Cell Tracker Far Red reagent (Invitrogen) for 30 min at 37 °C and 5% CO_2 in Eppendorf tubes. For the mixed culture, labelled or unlabelled 1.0×10^5 MDA-MB-436 and 1.0×10^5 MCF7 cells were combined and seeded in 24-well glass-bottom plates. After incubating for 2 h, cells were treated with 30 µl of various sEV suspensions: sEV-MDA, sEV-MCF7, sEV-MDA-Eu, sEV-MCF7-Eu or a PKH-negative control. The cells were incubated with the sEVs for 20 h, then washed with 1× PBS and fixed with 4% paraformaldehyde for 10 min. Following another wash with 1× PBS, cells were stained with DAPI for 10 min before LSCM analysis.

LSCM of sEV capture by cancer cells in the CTC detection experiment

MDA-MB-436 and MCF7 cells were seeded in six-well plates and cultured for 24 h, followed by treatment with 1.6×10^6 sEVs ml^{-1} of PKH67-labelled sEV-MDA-Tb or sEV-MCF7-Tb for 1-20 h to evaluate selective sEV capture and homotypic targeting. Cell nuclei were stained with DAPI at 37 °C for 10 min, and cells were rinsed three times with 1× PBS before LSCM imaging. PBMCs extracted from 1 ml of blood of healthy BALB/c nude mice were spiked with 30 CTC-like cells (MDA-MB-436), incubated in culture medium with 1 mM HAL for 3 h and then treated with PKH67-labelled sEV-MDA-Tb for 1 h in the presence of 0.8 µg ml^{-1} TCT at concentrations ranging from 4.0×10^4 sEVs ml^{-1} to 8.0×10^6 sEVs ml^{-1}. Cells were washed three times with 1× PBS, transferred onto a glass slide and analysed by LSCM. PpIX fluorescence, converted from HAL, was utilized to validate spiked CTC-like cells. This setup also confirmed the absence of sEV-MDA-Tb captured by PBMC components, including leucocytes. For CTC detection with signal amplification, PBMCs from 1 ml blood were spiked with 1–30 CTC-like cells (MDA-MB-436 cells) and incubated for 1 h with 0.8 µg ml^{-1} TCT and 1.6×10^6 sEVs ml^{-1} of HAL-loaded sEV-MDA-Tb. Uncaptured sEVs were removed by centrifugation at 300*g*, and the mixture was resuspended in 0.5 ml, disrupted by ultrasonication and introduced to approximately 2×10^6 MDA-MB-436 reporter cells. After 3 h incubation, cells were washed three times with 1× PBS and imaged by LSCM. Fluorescence intensities in Figs. 3d,i and 6e,f, Extended Data Figs. 2f–h and 3b and Supplementary Figs. 2d,f,h and 4b were calculated as the total fluorescence intensity from each cell divided by the number of cells ($n = 30–50$).

Preparation of TNBC-afflicted mice

BALB/c nude mice (female, obtained from Beijing Vital River Laboratory Animal Technology) were housed under specific pathogen-free conditions at the Pharmaceutical Animal Experimental Center at China

Pharmaceutical University, with a 12-h light–dark cycle, ambient temperature of 22 ± 2 °C and relative humidity of 50 ± 10%. The mice were injected with 1×10^6 MDA-MB-436 cells into the mammary fat pad to induce the TNBC xenograft and facilitate the spontaneous generation of CTCs. All mice were randomized, and their selection for injection or blood collection was conducted blindly.

Extraction of PBMCs and preparation of CTC-like cells

To prepare PBMCs, 2 ml of lymphocyte separation medium was introduced into a tube, with 1 ml of mouse anticoagulant blood gently layered on top. Following centrifugation at 500*g* for 30 min, the mononuclear cell layer was carefully collected. This layer underwent another centrifugation to isolate the PBMCs, followed by two washes with DMEM culture medium. The resulting PBMCs, obtained from 1 ml of blood, were combined with suspended MDA-MB-436 cells in DMEM supplemented with 10% sEV-depleted FBS and 1% PS. 8.0 µl of TCT solution (0.1 g ml^{-1}) with 1.6×10^6 sEVs ml^{-1} of sEV-MDA-Tb was added to the mixture and incubated for 1 h. The cells were washed with 1× PBS three times before imaging using LSCM.

Flow cytometry

Beckman Coulter's CytoFLEX LX, equipped with 405-nm, 488-nm, 561-nm and 638-nm lasers was used for all flow-cytometric measurements. For analysing host cells containing sEVs, the system was first calibrated using Beckman Coulter's CytoFLEX Daily QC Fluorospheres (lot no. 06AQD) following the manufacturer's protocol. The cell concentration was adjusted to 10^6–10^7 cells ml^{-1} by dilution with PBS. Once prepared, the sample was loaded into the instrument and analysed using the appropriate laser and detector settings according to the fluorescent dyes. The percentage of positive cells was determined by evaluating the fluorescence intensity of the cells.

Imaging flow cytometry

Imaging flow cytometry was performed using a virtual-freezing fluorescence imaging (VIFFI) system as previously described[40,41].The system comprises a microfluidic flow chip, a light-sheet excitation module, a scientific CMOS camera and an optical imaging system including an objective lens, a polygon scanner positioned at the Fourier plane and a tube lens. During operation, the polygon scanner counter-rotates relative to the flow to cancel cell motion on the camera, whereas a scanning light-sheet excitation beam limits local exposure (~10 µs) and ensures uniform illumination across the field of view. This configuration enables extended effective exposure times and high-sensitivity fluorescence imaging at high flow speeds. Continuous imaging is achieved through synchronized scanner rotation and camera acquisition, allowing high-throughput image capture at more than 10,000 events per second. This approach enables microscopy-grade fluorescence imaging of cells in flow and improves detection sensitivity through spatially resolved fluorescence analysis. Captured images were analysed using custom code described in the original report[40,41]. Although VIFFI was used in this study, the liquid biopsy techniques described here are compatible with other, including commercially available, imaging flow cytometry systems. Such systems can enhance detection sensitivity at the single-cell level by leveraging image-based features rather than one-dimensional fluorescence intensity.

Analysis of sEVs from cell lines with flow cytometry and imaging flow cytometry

We assessed sEV-MDA, sEV-MCF7 and sEV-BLD derived from cancer cell line culture mediums and serum using both the conventional flow cytometer (CytoFLEX LX, Beckman Coulter) and the imaging flow cytometer (VIFFI flow cytometer). This was done to validate our method's capability to distinguish sEV-MDA from other serum- or cancer-derived sEVs. Initially, we extracted the sEV-MDA, sEV-MCF7 and sEV-BLD from MDA-MB-436, MCF7 culture mediums and FBS, respectively. These sEVs were subsequently stained with PKH67 and modified by Eu^{3+}, forming sEV-MDA-Eu, sEV-MCF7-Eu and sEV-BLD-Eu. These stained sEVs, both individually and in mixtures, were then allowed to interact with host cells (MDA-MB-436 cells) over a 3-h incubation period. After incubation, sEV-marked host cells were detached using trypsin, thrice rinsed with 1× PBS, suspended in 1× PBS at a density of approximately 1.0×10^7 cells ml^{-1} and finally analysed using both flow-cytometric methods. For flow cytometry, host cells labelled with sEVs were enumerated on the basis of PKH67 fluorescence. For imaging flow cytometry, the number of host cells labelled with sEVs was determined on the basis of the identification of PKH67 fluorescence regions in the images of host cells.

Analysis of sEVs from TNBC tumour cells with flow cytometry and imaging flow cytometry

To selectively analyse sEVs derived from TNBC, we executed the following steps: (1) sEVs were isolated via centrifugation from 1.0-ml serum samples, each prepared by pooling serum from two mice, collected from healthy mice, TNBC-afflicted mice and Taxol-treated TNBC-afflicted mice. (2) These sEV mixtures were subsequently labelled with PKH67 and Eu^{3+}. (3) The stained sEVs were then incubated with host cells (MDA-MB-436 cells) for 3 h. (4) After incubation, cells were detached using trypsin, rinsed thrice with 1× PBS and then suspended in 1× PBS at a density of approximately 1.0×10^7 cells ml^{-1}. (5) These samples were subsequently analysed using both the flow cytometer (CytoFLEX LX, Beckman Coulter) and the imaging flow cytometer (VIFFI flow cytometer). The *P* values for the results of both types of flow cytometry were calculated on the basis of a two-sided *t*-test (Prism, GraphPad) between healthy mice and TNBC-afflicted mice to assess the difference between the two groups.

Analysis of CTC-like cells with flow cytometry

We assessed CTC-like cells from the MDA-MB-436 cell line using the flow cytometer (CytoFLEX LX, Beckman Coulter). The purpose of this assessment was to validate our method's capability to detect single CTC-like cells from PBMCs. Initially, a known number of CTC-like cells (1–20 cells) was added to the PBMCs isolated from whole blood samples. The PBMCs with CTC-like cells were then incubated with a culture medium containing 0.8 µg ml^{-1} TCT and 1.6×10^6 sEVs ml^{-1} of HAL-loaded sEV-MDA-Tb for 1 h. Following centrifugation at 300*g* for 3 min to discard uncaptured sEVs, the mixture was resuspended in 0.5 ml of cell culture medium. Subsequently, the cells were disrupted by ultrasonication and introduced to approximately 2×10^6 MDA-MB-436 cells as reporter cells seeded in a dish. After a 3-h incubation, the cells were detached using trypsin followed by washing three times with 1× PBS and suspension in 1× PBS at a density of approximately 1.0×10^7 cells ml^{-1}. Finally, the reporter cells were enumerated using flow cytometry on the basis of PpIX fluorescence.

Analysis of CTCs derived from TNBC tumour cells with flow cytometry

To detect and enumerate CTCs derived from a TNBC tumour, we executed the following steps: (1) PBMCs were extracted from 1.0-ml whole blood samples of healthy mice, TNBC-afflicted mice and Taxol-treated TNBC-afflicted mice via centrifugation. (2) The cells were subsequently incubated with a culture medium containing 0.8 µg ml^{-1} TCT and 1.6×10^6 sEVs ml^{-1} of HAL-loaded sEV-MDA-Tb for 1 h. (3) The mixture was centrifuged at 300*g* for 3 min to remove uncaptured sEVs. (4) These samples were resuspended in 0.5 ml of cell culture medium and subjected to ultrasonication for cell disruption. (5) After ultrasonication, the contents were transferred to a dish containing approximately 2×10^6 MDA-MB-436 cells as reporter cells. (6) After a 3-h incubation, the cells were detached using trypsin and rinsed thrice with 1× PBS and then suspended in 1× PBS at a density of approximately 1.0×10^7 cells ml^{-1}. (7) The reporter cell samples were subsequently analysed using the flow

cytometer (CytoFLEX LX, Beckman Coulter). The *P* values for the flow cytometry results were calculated on the basis of a two-sided *t*-test (Prism, GraphPad) between healthy mice and TNBC-afflicted mice to assess the difference between the two groups. Meanwhile, processes without cell disruption were also analysed to demonstrate that the cell disruption process is essential for the highly sensitive detection of CTCs (Extended Data Fig. 7).

Analysis of sEVs and CTCs for clinical samples

Patients were recruited on the basis of a clinical diagnosis of TNBC, confirmed by pathological assessment showing negative expression of ER, PR and HER2. A total of 13 female patients were enrolled, with a median age of 55 years (range of 35–65 years) and clinical stages ranging from I to III (Extended Data Tables 1 and 2). In addition, 13 healthy female subjects were also recruited as controls for comparison. Before blood collection, the patients had undergone various degrees of treatment, including surgery, radiotherapy, chemotherapy and targeted therapy. It should be noted that these therapeutic interventions may have a certain impact on the detection results.

Ethics statement. All animal experiments were approved by the Pharmaceutical Animal Experimental Center at China Pharmaceutical University (no. 220201299) and were conducted in accordance with institutional guidelines for animal care and use. Human sample collection and related experiments were approved by the Ethics Committee of Nanjing Hospital of Chinese Medicine affiliated with Nanjing University of Chinese Medicine (KY2024088). Informed consent was obtained from all participants, who voluntarily provided blood samples without compensation. All procedures were performed in accordance with relevant ethical regulations.

Reporting summary

Further information on research design is available in the Nature Portfolio Reporting Summary linked to this Article.

Data availability

All relevant data supporting the findings of this study are available within the Article and its Supplementary Information. Source data are provided with this paper.

References

1. Fang, R. H., Kroll, A. V., Gao, W. & Zhang, L. Cell membrane coating nanotechnology. *Adv. Mater.* **30**, e1706759 (2018).
2. Cao, Y. et al. Molecular characterization of exosomes for subtype-based diagnosis of breast cancer. *J. Am. Chem. Soc.* **144**, 13475–13486 (2022).
3. Zhang, L. M. et al. Homotypic targeting delivery of siRNA with artificial cancer cells. *Adv. Healthc. Mater.* **9**, e1900772 (2020).
4. Glinsky, V. V. et al. Intravascular metastatic cancer cell homotypic aggregation at the sites of primary attachment to the endothelium. *Cancer Res.* **63**, 3805–3811 (2003).
5. Fang, R. H. et al. Cancer cell membrane-coated nanoparticles for anticancer vaccination and drug delivery. *Nano Lett.* **14**, 2181–2188 (2014).
6. Honig, B. & Shapiro, L. Adhesion protein structure, molecular affinities, and principles of cell–cell recognition. *Cell* **181**, 520–535 (2020).
7. Nose, A., Mahajan, V. B. & Goodman, C. S. Connectin: a homophilic cell-adhesion molecule expressed on a subset of muscles and the motoneurons that innervate them in *Drosophila*. *Cell* **70**, 553–567 (1992).
8. Katsamba, P. et al. Linking molecular affinity and cellular specificity in cadherin-mediated adhesion. *Proc. Natl Acad. Sci. USA* **106**, 11594–11599 (2009).
9. Martin, G. M. et al. Affinity-matured homotypic interactions induce spectrum of PfCSP structures that influence protection from malaria infection. *Nat. Commun.* **14**, 4546 (2023).
10. Imkeller, K. et al. Antihomotypic affinity maturation improves human B cell responses against a repetitive epitope. *Science* **360**, 1358–1362 (2018).
11. Ravasco, J., Paiva-Santos, A. C. & Conde, J. Technological challenges of biomembrane-coated top-down cancer nanotherapy. *Nat. Rev. Bioeng.* **1**, 156–158 (2023).
12. Qu, Y. et al. Cancer-cell-biomimetic nanoparticles for targeted therapy of multiple myeloma based on bone marrow homing. *Adv. Mater.* **34**, e2107883 (2022).
13. Elsharkasy, O. M. et al. Extracellular vesicles as drug delivery systems: why and how? *Adv. Drug Deliv. Rev.* **159**, 332–343 (2020).
14. Fang, R. H., Gao, W. & Zhang, L. Targeting drugs to tumours using cell membrane-coated nanoparticles. *Nat. Rev. Clin. Oncol.* **20**, 33–48 (2023).
15. Bajaj, P., Schweller, R. M., Khademhosseini, A., West, J. L. & Bashir, R. 3D biofabrication strategies for tissue engineering and regenerative medicine. *Annu. Rev. Biomed. Eng.* **16**, 247–276 (2014).
16. Khademhosseini, A., Langer, R., Borenstein, J. & Vacanti, J. P. Microscale technologies for tissue engineering and biology. *Proc. Natl Acad. Sci. USA* **103**, 2480–2487 (2006).
17. Sabatos, C. A. et al. A synaptic basis for paracrine interleukin-2 signaling during homotypic T cell interaction. *Immunity* **29**, 238–248 (2008).
18. Gérard, A., Cope, A., Kemper, C., Alon, R. & Köchl, R. LFA-1 in T cell priming, differentiation, and effector functions. *Trends Immunol.* **42**, 706–722 (2021).
19. Büll, C., Stoel, M. A., den Brok, M. H. & Adema, G. J. Sialic acids sweeten a tumor's life. *Cancer Res.* **74**, 3199–3204 (2014).
20. Cui, H. X., Lin, Y., Yue, L. L., Zhao, X. M. & Liu, J. C. Differential expression of the α2,3-sialic acid residues in breast cancer is associated with metastatic potential. *Oncol. Rep.* **25**, 1365–1371 (2011).
21. Hait, N. C. et al. Extracellular sialyltransferase st6gal1 in breast tumor cell growth and invasiveness. *Cancer Gene Ther.* **29**, 1662–1675 (2022).
22. Zhang, M. H. et al. Engineered exosomes from different sources for cancer-targeted therapy. *Signal Transduct. Target. Ther.* **8**, 124 (2023).
23. Ma, Y. F. et al. Engineering therapeutical extracellular vesicles for clinical translation. *Trends Biotechnol.* **43**, 61–82 (2025).
24. Foulkes, W. D., Smith, I. E. & Reis-Filho, J. S. Triple-negative breast cancer. *N. Engl. J. Med.* **363**, 1938–1948 (2010).
25. Wang, J. L. et al. Lanthanide complexes for tumor diagnosis and therapy by targeting sialic acid. *ACS Nano* **16**, 14827–14837 (2022).
26. Van Niel, G., D'Angelo, G. & Raposo, G. Shedding light on the cell biology of extracellular vesicles. *Nat. Rev. Mol. Cell Biol.* **19**, 213–228 (2018).
27. Mathieu, M., Martin-Jaular, L., Lavieu, G. & Théry, C. Specificities of secretion and uptake of exosomes and other extracellular vesicles for cell-to-cell communication. *Nat. Cell Biol.* **21**, 9–17 (2019).
28. Jeppesen, D. K. et al. Reassessment of exosome composition. *Cell* **177**, 428–445.e418 (2019).
29. Maas, S. L. N., Breakefield, X. O. & Weaver, A. M. Extracellular vesicles: unique intercellular delivery vehicles. *Trends Cell Biol.* **27**, 172–188 (2017).
30. Welsh, J. A. et al. Minimal information for studies of extracellular vesicles (MISEV2023): from basic to advanced approaches. *J. Extracell. Vesicles* **13**, e12404 (2024).
31. Yu, W. et al. Exosome-based liquid biopsies in cancer: opportunities and challenges. *Ann. Oncol.* **32**, 466–477 (2021).

32. Lee, Y. J. et al. Recent advances of small extracellular vesicle biomarkers in breast cancer diagnosis and prognosis. *Mol. Cancer* **22**, 33 (2023).
33. Kosaka, N. et al. Exploiting the message from cancer: the diagnostic value of extracellular vesicles for clinical applications. *Exp. Mol. Med.* **51**, 1–9 (2019).
34. Wan, J. C. M., Sasieni, P. & Rosenfeld, N. Promises and pitfalls of multi-cancer early detection using liquid biopsy tests. *Nat. Rev. Clin. Oncol.* **22**, 566–580 (2025).
35. McKiernan, J. et al. A novel urine exosome gene expression assay to predict high-grade prostate cancer at initial biopsy. *JAMA Oncol.* **2**, 882–889 (2016).
36. van Niel, G. et al. Challenges and directions in studying cell–cell communication by extracellular vesicles. *Nat. Rev. Mol. Cell Biol.* **23**, 369–382 (2022).
37. Liu, W. Z., Ma, Z. J. & Kang, X. W. Current status and outlook of advances in exosome isolation. *Anal. Bioanal. Chem.* **414**, 7123–7141 (2022).
38. Xiong, H. W. et al. Recent progress in detection and profiling of cancer cell-derived exosomes. *Small* **17**, 2007971 (2021).
39. Xu, L. Z. et al. Optical, electrochemical and electrical (nano) biosensors for detection of exosomes: a comprehensive overview. *Biosens. Bioelectron.* **161**, 112222 (2020).
40. Mikami, H. et al. Virtual-freezing fluorescence imaging flow cytometry. *Nat. Commun.* **11**, 1162 (2020).
41. Isozaki, A. et al. Intelligent image-activated cell sorting 2.0. *Lab Chip* **20**, 2263–2273 (2020).
42. Hibbert, D. B. & Gooding, J. J. *Data Analysis for Chemistry* (Oxford Univ. Press, 2005).
43. Filby, A. & Carpenter, A. E. A new image for cell sorting. *N. Engl. J. Med.* **386**, 1755–1758 (2022).
44. Fujino, S. et al. Abstract 87: Targeting POU5F1-expressing circulating tumor cells to prevent metastasis and recurrence in colorectal cancer. *Cancer Res.* **85**, 87–87 (2025).
45. Fang, C. T., Kuo, H. H., Yuan, C. J., Yao, J. S. & Yih, L. H. Mdivi-1 induces spindle abnormalities and augments taxol cytotoxicity in MDA-MB-231 cells. *Cell Death Discov.* **7**, 118 (2021).
46. Steeg, P. S. Tumor metastasis: mechanistic insights and clinical challenges. *Nat. Med.* **12**, 895–904 (2006).
47. Cristofanilli, M. et al. Circulating tumor cells, disease progression, and survival in metastatic breast cancer. *N. Engl. J. Med.* **351**, 781–791 (2004).
48. Gupta, G. P. & Massagué, J. Cancer metastasis: building a framework. *Cell* **127**, 679–695 (2006).
49. Allard, W. J. et al. Tumor cells circulate in the peripheral blood of all major carcinomas but not in healthy subjects or patients with nonmalignant diseases. *Clin. Cancer Res.* **10**, 6897–6904 (2004).
50. Chudziak, J. et al. Clinical evaluation of a novel microfluidic device for epitope-independent enrichment of circulating tumour cells in patients with small cell lung cancer. *Analyst* **141**, 669–678 (2016).
51. Nagrath, S. et al. Isolation of rare circulating tumour cells in cancer patients by microchip technology. *Nature* **450**, 1235–1239 (2007).
52. Hajba, L. & Guttman, A. Circulating tumor-cell detection and capture using microfluidic devices. *Trends Anal. Chem.* **59**, 9–16 (2014).
53. Cossarizza, A. et al. Guidelines for the use of flow cytometry and cell sorting in immunological studies (second edition). *Eur. J. Immunol.* **49**, 1457–1973 (2019).
54. Gorges, T. M. et al. Circulating tumour cells escape from EpCAM-based detection due to epithelial-to-mesenchymal transition. *BMC Cancer* **12**, 178 (2012).
55. Matsumura, H. et al. Virtual-freezing fluorescence imaging flow cytometry with 5-aminolevulinic acid stimulation and antibody labeling for detecting all forms of circulating tumor cells. *Lab Chip* **23**, 1561–1575 (2023).
56. Lim, S. B., Di Lee, W., Vasudevan, J., Lim, W. T. & Lim, C. T. Liquid biopsy: one cell at a time. *npj Precis. Oncol.* **3**, 23 (2019).
57. Donnenberg, A. D. & Donnenberg, V. S. Rare-event analysis in flow cytometry. *Clin. Lab. Med.* **27**, 627–652 (2007).
58. Andree, K. C., van Dalum, G. & Terstappen, L. Challenges in circulating tumor cell detection by the CellSearch system. *Mol. Oncol.* **10**, 395–407 (2016).
59. Daneshmand, S. et al. Hexaminolevulinate blue-light cystoscopy in non-muscle-invasive bladder cancer: review of the clinical evidence and consensus statement on appropriate use in the USA. *Nat. Rev. Urol.* **11**, 589–596 (2014).
60. MacGregor, M. et al. Cancer cell detection device for the diagnosis of bladder cancer from urine. *Biosens. Bioelectron.* **171**, 112699 (2021).
61. Pich, O. et al. The evolution of hematopoietic cells under cancer therapy. *Nat. Commun.* **12**, 4803 (2021).
62. Beadle, G., Baade, P. & Fritschi, L. Acute myeloid leukemia after breast cancer: a population-based comparison with hematological malignancies and other cancers. *Ann. Oncol.* **20**, 103–109 (2009).
63. Ding, T. et al. Image-activated cell sorting. *Nat. Rev. Bioeng.* **3**, 890–907 (2025).
64. Hao, Y. et al. Extracellular vesicles from antler blastema progenitor cells reverse bone loss and mitigate aging-related phenotypes in mice and macaques. *Nat. Aging* **5**, 1790–1809 (2025).
65. Chen, X. et al. Small extracellular vesicles from young plasma reverse age-related functional declines by improving mitochondrial energy metabolism. *Nat. Aging* **4**, 814–838 (2024).
66. Wu, M. et al. Surface-layer protein-enhanced immunotherapy based on cell membrane-coated nanoparticles for the effective inhibition of tumor growth and metastasis. *ACS Appl. Mater. Interfaces* **11**, 9850–9859 (2019).
67. Robey, R. W. et al. Revisiting the role of ABC transporters in multidrug-resistant cancer. *Nat. Rev. Cancer* **18**, 452–464 (2018).
68. Théry, C., Amigorena, S., Raposo, G. & Clayton, A. Isolation and characterization of exosomes from cell culture supernatants and biological fluids. *Curr. Protoc. Cell Biol.* **30**, 3221–32229 (2006).

Acknowledgements

This work was mainly supported by the JSPS Core-to-Core Program grant no. JPJSCCA20190007 (K.G.), the JSPS KAKENHI Programs grant nos. JP19H05633 (K.G.), JP20H00317 (K.G.), JP21H05047 (S.S.), JP20KK0341 (S.S.), JP20H03252 (S.S.) and JP24K17800 (T.D.), the JST START Program grant no. JPMJST2115 (M.S., K.G.), the JST CREST Programs grant nos. JPMJCR1863 (S.S.) and JPMJCR24B3 (S.S.), the JST ASPIRE Program grant no. JPMJAP2316 (K.G.), the JST EXPERT-J program (D.D.C, K.G.), the AMED grant no. 22ak0101163h0002 (M.S., K.G.), the MEXT Quantum Leap Flagship Program grant no. JPMXS0120330644 (K.G.), XPRIZE Foundation (K.G.), KAKETSUKEN (K.G.), White Rock Foundation (K.G.), G-7 Scholarship Foundation (M.S., K.G.) and China Scholarship Council grant no. 202107060015 (H.-S.W.). Additional support was provided by Horizon Europe through the Marie Skłodowska-Curie Actions Staff Exchanges project EXPLORER grant no. 101235654 (P.P.), the Deanship of Scientific Research at King Saud University through the RICSP Program (grant no. MbSC2030), the Mohammed bin Salman Center for Future Science and Technology for Saudi-Japan Vision 2030 (K.G. and A.A.) and the Cell Aging Control Endowed Chair at the University of Tokyo (K.G.). The funders had no role in study design, data collection and analysis, decision to publish or preparation of the manuscript. We thank the staff in the FACS Core Laboratory at the University of Tokyo and C. Wang (Department of Clinical Laboratory, Nanjing Hospital of Chinese Medicine, affiliated with Nanjing University of Chinese Medicine) for collecting the clinical samples.

Author contributions

H.-S.W., T.D., Y.L. and K.G. conceived and refined the idea. H.-S.W. and Hy.M. conducted the sEV surface modification and homotypic targeting enhancement experiments. H.-S.W. and T.D. designed and led the validation using clinical samples. X.-Y.H., Z.-W.Y, J.-L.S., Y.-Y.Y., F.-H.G. and J.-J.L. performed the animal experiments. H.-S.W., Y.L, Ya.Z., M.H., N.T.I., Hk.M., A.U. and H.G. conducted the flow cytometry and imaging flow cytometry experiments. H.-S.W., T.D., Yu.Z., Ya.Z. and K.G. analysed and interpreted the experimental data. H.-S.W., T.D., Yu.Z. and K.G. wrote the Article. F.L., Y.K., P.P., A.T., K.S., Y.I., T.U., M.S., D.D.C. and S.S. provided valuable comments to improve the quality of the work. All authors participated in reviewing the Article. K.G. obtained most funding and supervised the work.

Competing interests

H.-S.W., T.D., Y.L., S.S. and K.G. are inventors on a patent application (PCT/JP2025/005688) covering the sEV detection method. K.G. is an inventor on a patent covering the VIFFI imaging flow cytometer (patent nos. JP6881778 and US10890520B2). T.D. and K.G. are shareholders of NanoTitan. N.N. and K.G. are shareholders of CYBO. M.S. and K.G. are shareholders of FlyWorks. The other authors declare no competing interests.

Additional information

Extended data is available for this paper at https://doi.org/10.1038/s41551-026-01743-2.

Supplementary information The online version contains supplementary material available at https://doi.org/10.1038/s41551-026-01743-2.

Correspondence and requests for materials should be addressed to Keisuke Goda.

Peer review information *Nature Biomedical Engineering* thanks Hsian-Rong Tseng and the other, anonymous, reviewer(s) for their contribution to the peer review of this work. Peer reviewer reports are available.

[1]Department of Chemistry, The University of Tokyo, Tokyo, Japan. [2]Department of Pharmaceutical Analysis, China Pharmaceutical University, Nanjing, China. [3]SiRIUS Institute of Medical Research, Tohoku University, Sendai, Japan. [4]NanoTitan, Tokyo, Japan. [5]Department of Biological Sciences, Nazarbayev University, Astana, Kazakhstan. [6]Department of Biotechnology and Bioengineering, Huaqiao University, Amoy, China. [7]Department of Physics, Politecnico di Milano, Milano, Italy. [8]Department of Obstetrics and Gynecology, Graduate School of Medicine, The University of Tokyo, Tokyo, Japan. [9]Breast Oncology Center, The Cancer Institute Hospital of Japanese Foundation for Cancer Research, Tokyo, Japan. [10]King Abdullah Institute for Nanotechnology, King Saud University, Riyadh, Saudi Arabia. [11]CYBO, Tokyo, Japan. [12]Department of Clinical Laboratory Medicine, The University of Tokyo, Tokyo, Japan. [13]Institute for Genetic Medicine, Hokkaido University, Sapporo, Japan. [14]Global Station for Biosurfaces and Drug Discovery, Hokkaido University, Sapporo, Japan. [15]Department of Bioengineering, University of California, Los Angeles, CA, USA. [16]Department of Mechanical and Aerospace Engineering, University of California, Los Angeles, CA, USA. [17]California NanoSystems Institute, University of California, Los Angeles, CA, USA. [18]EXPERT-GRI Promotion Office, The University of Tokyo, Tokyo, Japan. [19]Division of Biological Science, Nara Institute of Science and Technology, Ikoma, Japan. [20]Data Science Center, Nara Institute of Science and Technology, Ikoma, Japan. [21]Center for Digital Green Innovation, Nara Institute of Science and Technology, Ikoma, Japan. [22]Medilux Research Center, Nara Institute of Science and Technology, Ikoma, Japan. [23]Institute of Technological Sciences, Wuhan University, Wuhan, China. [24]Graduate School of Medicine, Tohoku University, Sendai, Japan. [25]International Center for Synchrotron Radiation Innovation Smart, Tohoku University, Sendai, Japan. [26]These authors contributed equally: Huai-Song Wang, Tianben Ding, Yuhong Liu. ✉e-mail: goda@chem.s.u-tokyo.ac.jp

https://doi.org/10.1038/s41551-026-01743-2

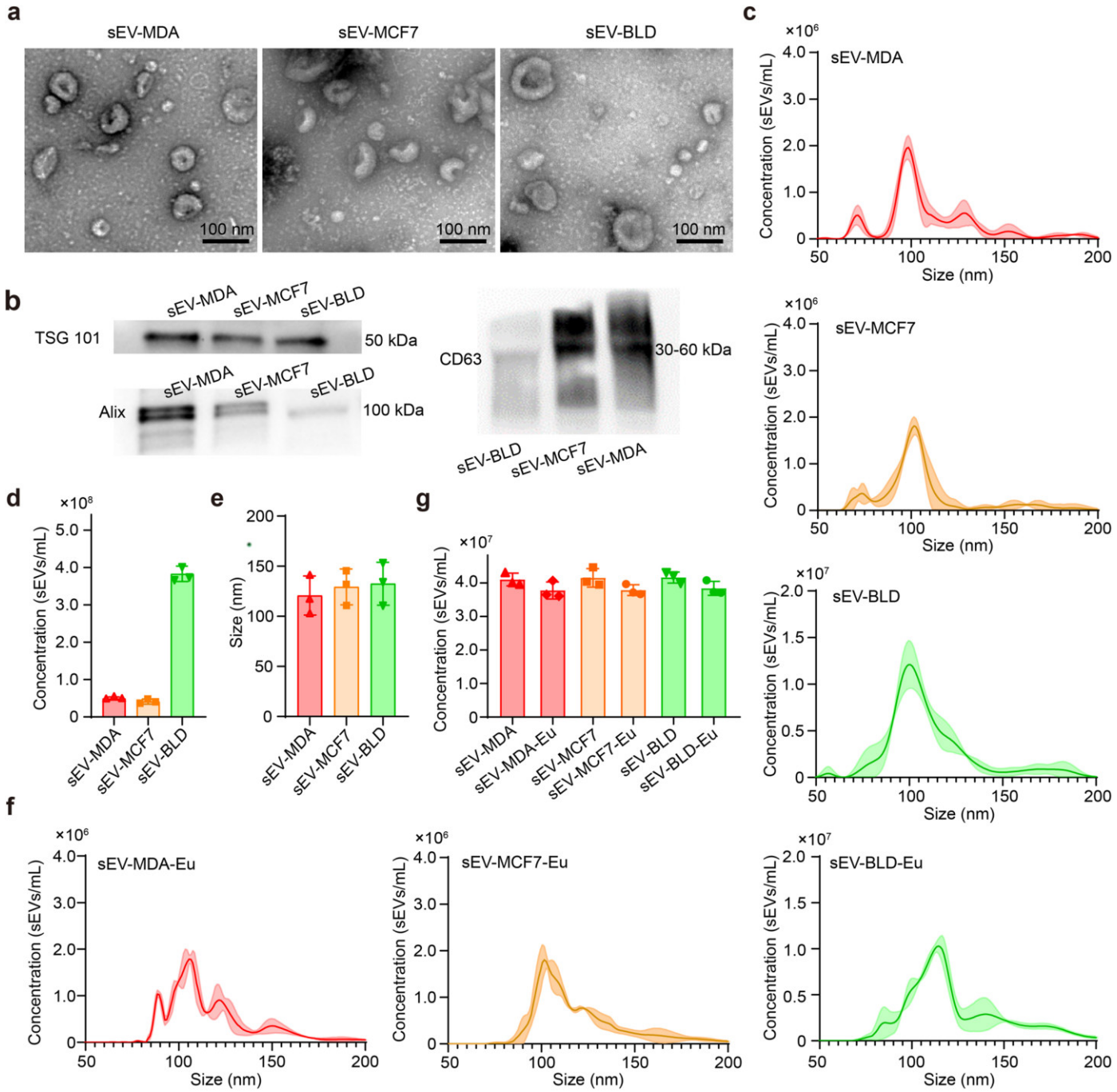

Extended Data Fig. 1 | Characterization of sEVs. a, Transmission electron microscope (TEM) images of sEVs. **b**, Western blotting (WB) analysis of sEV proteins: TSG101, Alix, and CD63. sEVs were diluted to a concentration of approximately 4.0×10^7 sEVs/ml. **c**, Concentrations of sEV-MDA, sEV-MCF7, and sEV-BLD measured by nanoparticle tracking analysis. Solid lines indicate the mean, while shaded areas show the range of maximum and minimum concentrations observed across three independent experiments. **d**, Accumulated concentrations of sEVs ranging from 50 to 200 nm in size. Data are presented as mean ± standard deviation (n = 3 independent samples). **e**, Hydrodynamic sizes of sEVs. Data are presented as mean ± standard deviation (n = 3 independent samples). **f**, Concentrations of sEV-MDA-Eu, sEV-MCF7-Eu, and sEV-BLD-Eu measured by nanoparticle tracking analysis. Solid lines indicate the mean, while shaded areas show the range of maximum and minimum concentrations observed across three independent experiments. **g**, Comparison of sEV-MDA, sEV-MCF7, and sEV-BLD concentrations before and after Eu^{3+} ion-based surface modification. For this validation, the concentration of sEV-BLD before modification was adjusted to match those of sEV-MDA and sEV-MCF7 to enable a fair comparison of the effects of surface modification under equivalent conditions. Data are presented as mean ± standard deviation (n = 3 independent samples).

https://doi.org/10.1038/s41551-026-01743-2

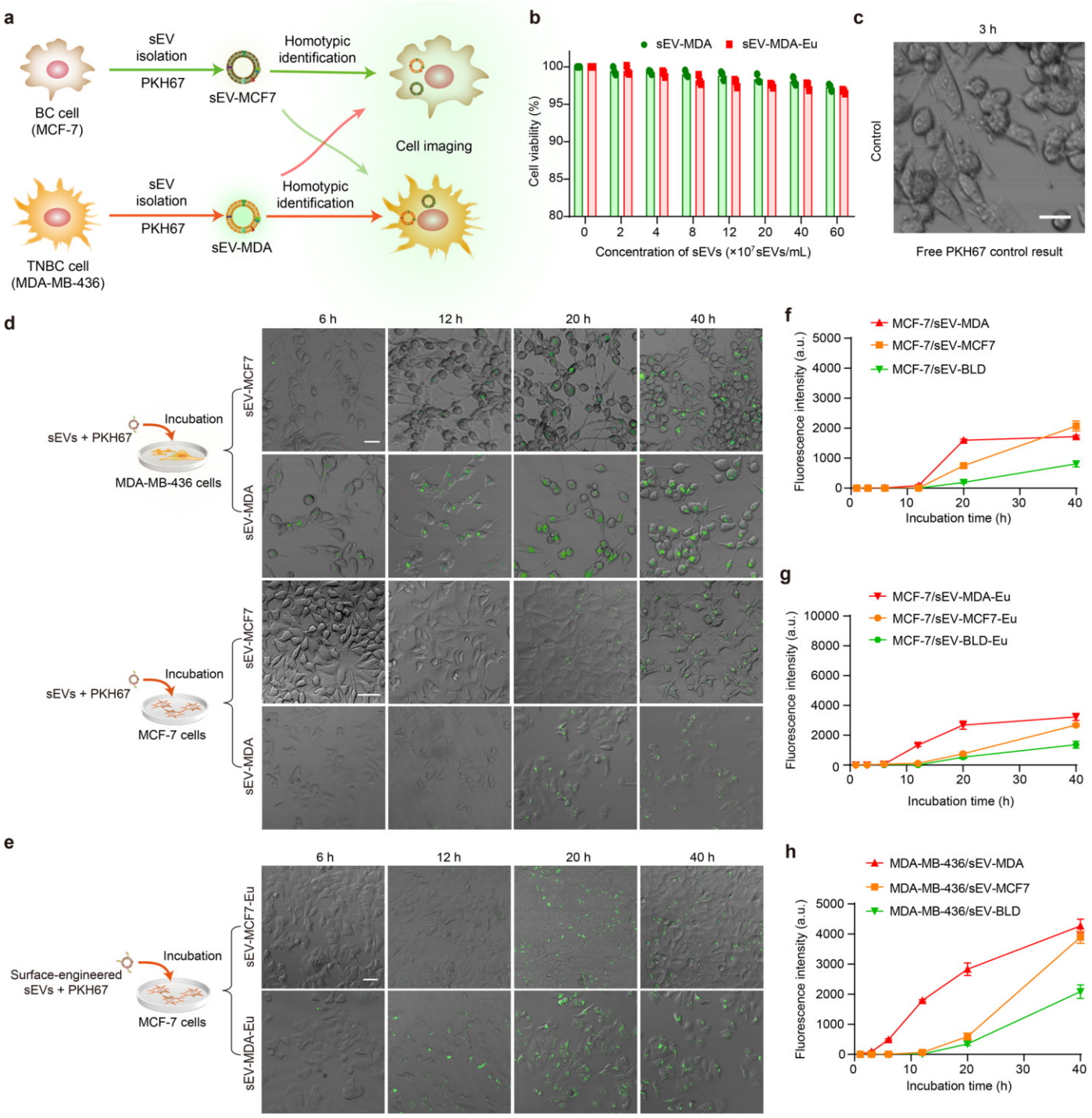

Extended Data Fig. 2 | See next page for caption.

https://doi.org/10.1038/s41551-026-01743-2

Extended Data Fig. 2 | Cellular sEV-mediated homotypic targeting. a, Method for investigating the homotypic recognition of TNBC- and BC-derived sEVs. **b**, Cytotoxicity analysis of sEV-MDA and sEV-MDA-Eu tested by an MTT toxicity assay. MDA-MB-436 cells were incubated in growth medium with 10% FBS containing different concentrations of sEV-MDA or sEV-MDA-Eu for 24 h. After being washed twice with 200 µL of PBS, the cells were incubated in 100 µL of PBS containing 1 mg/ml MTT for 4 h and were then subjected to the standard MTT assay. Cell viabilities are presented as mean ± standard deviation (n = 3 independent samples). **c**, MDA-MB-436 cells after a 3-h incubation with culture medium prepared by adding PKH67 to sEV-depleted medium followed by ultracentrifugation. The fluorescence-free field of view confirms the absence of nonspecific PKH67 binding or dye aggregation on cells during the sEV capture process. Scale bar, 40 µm. **d**, MDA-MB-436 cells incubated with sEV-MCF7 or sEV-MDA. Scale bar, 30 µm. MCF7 cells incubated with sEV-MCF7 or sEV-MDA. Scale bar, 40 µm. The concentration of the sEV-MCF7 or sEV-MDA suspension is ~4.0×10^7 sEVs/ml. The MDA-MB-436 and MCF7 cells, seeded in confocal dishes, were incubated with 20 µL sEV-MCF7 or sEV-MDA suspension for varying durations between 6 h and 40 h. Then, the cells were washed with 1× PBS and subsequently subjected to LSCM analysis. **e**, MCF7 cells incubated with sEV-MCF7-Eu or sEV-MDA-Eu for 6-40 h. The concentration of the sEV-MCF7-Eu or sEV-MDA-Eu suspension is ~4.0×10^7 sEVs/mL. The MCF7 cells, seeded in confocal dishes, were incubated with the 20 µL sEV-MCF7-Eu or sEV-MDA-Eu suspension for varying durations between 6 h and 40 h. Then, the cells were washed with 1× PBS and subsequently subjected to confocal microscopy analysis. Scale bar: 40 µm. **f**, Relationship between the incubation time (1-40 h) and fluorescence intensity of MCF7 cells incubated with sEV-MDA (20 µL), sEV-MCF7 (20 µL), or sEV-BLD (20 µL). Data are presented as mean ± standard deviation (n = 5 independent samples). **g**, Surface-engineered sEV capture for sEV-MCF7-Eu, sEV-MDA-Eu, and sEV-BLD-Eu by MCF7 cells. Data are presented as mean ± standard deviation (n = 5 independent samples). **h**, Relationship between the incubation time (1-40 h) and fluorescence intensity of MDA-MB-436 cells incubated with sEV-MDA (20 µL), sEV-MCF7 (20 µL), or sEV-BLD (20 µL). Data are presented as mean ± standard deviation (n = 5 independent samples).

https://doi.org/10.1038/s41551-026-01743-2

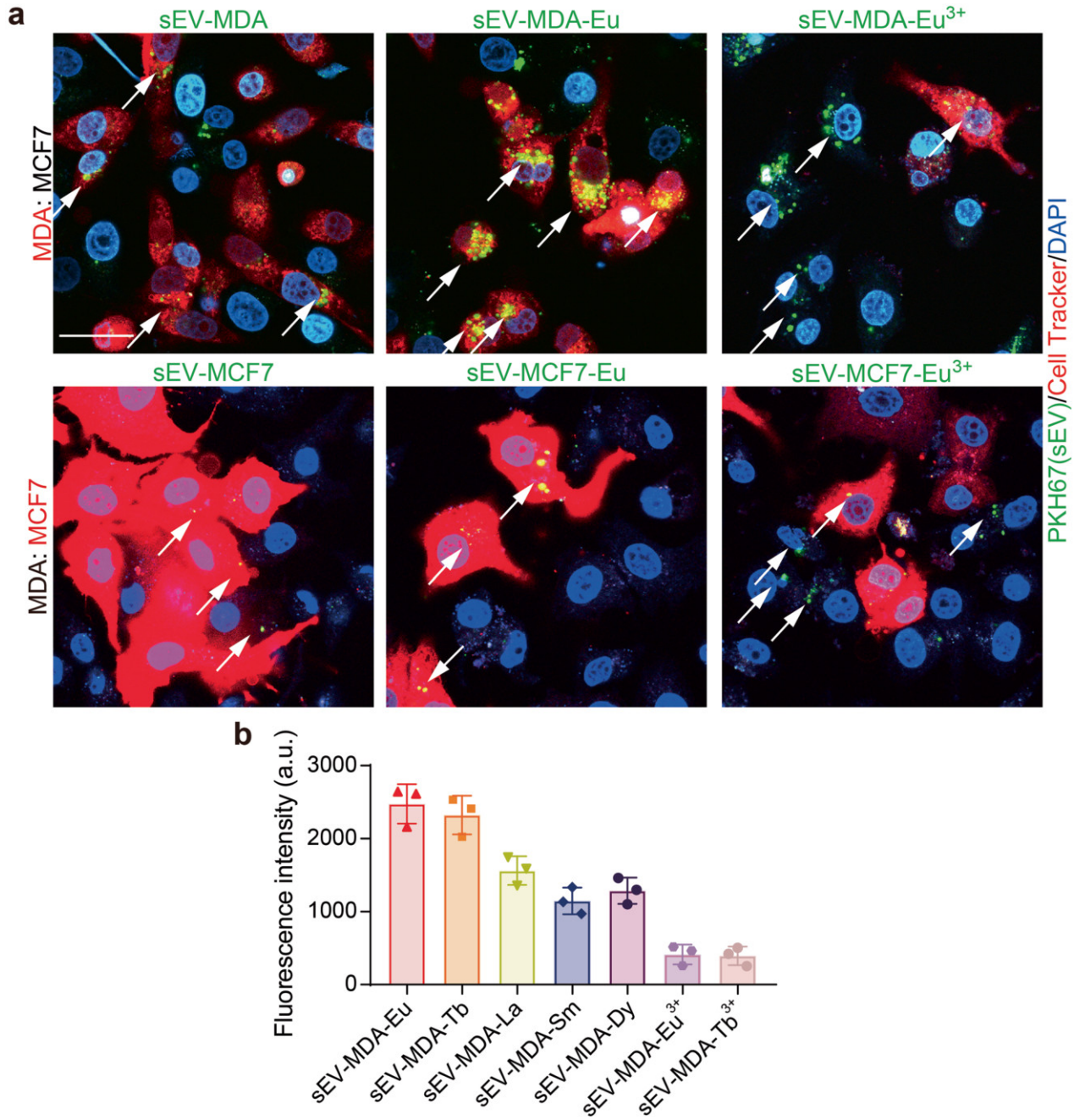

Extended Data Fig. 3 | LSCM of mixed and MDA-MB-436 cells incubated with various sEVs. a, LSCM-based monitoring of mixed cell cultures, with and without cell-tracker labelling of MDA-MB-436 and MCF7 cells, after 20-h incubation with (top) sEV-MDA, sEV-MDA-Eu (sEV-MDA modified by TCE) or sEV-MDA-Eu^{3+} (sEV-MDA directly incubated with $EuCl_3$), and (bottom) sEV-MCF7, sEV-MCF7-Eu (sEV-MCF7 modified by TCE) or sEV-MCF7-Eu^{3+} (sEV-MCF7 directly incubated with $EuCl_3$). Arrows indicate sEVs captured by cells. Scale bars: 20 μm. **b**, Intensity of fluorescence emitted from the captured sEVs per host MDA-MB-436 cell after incubation with different sEV-MDA-Ln samples (sEV-MDA modified with various lanthanide ions). The preparation of sEV-MDA-Tb, sEV-MDA-La, sEV-MDA-Sm, and sEV-MDA-Dy followed the same procedure as that of sEV-MDA-Eu, except that the Eu in TCE was replaced with Tb, La, Sm, or Dy, respectively. For sEV-MDA-Eu^{3+} and sEV-MDA-Tb^{3+}, the preparation process was identical to that of sEV-MDA-Eu and sEV-MDA-Tb, except that TCE and TCT were substituted with $EuCl_3$ and $TbCl_3$, respectively. Data are presented as mean ± standard deviation (n = 3 independent samples). Fluorescence intensity values shown in this figure were obtained by calculating the total fluorescence intensity from each cell and dividing it by the total number of cells (n = 30-50).

https://doi.org/10.1038/s41551-026-01743-2

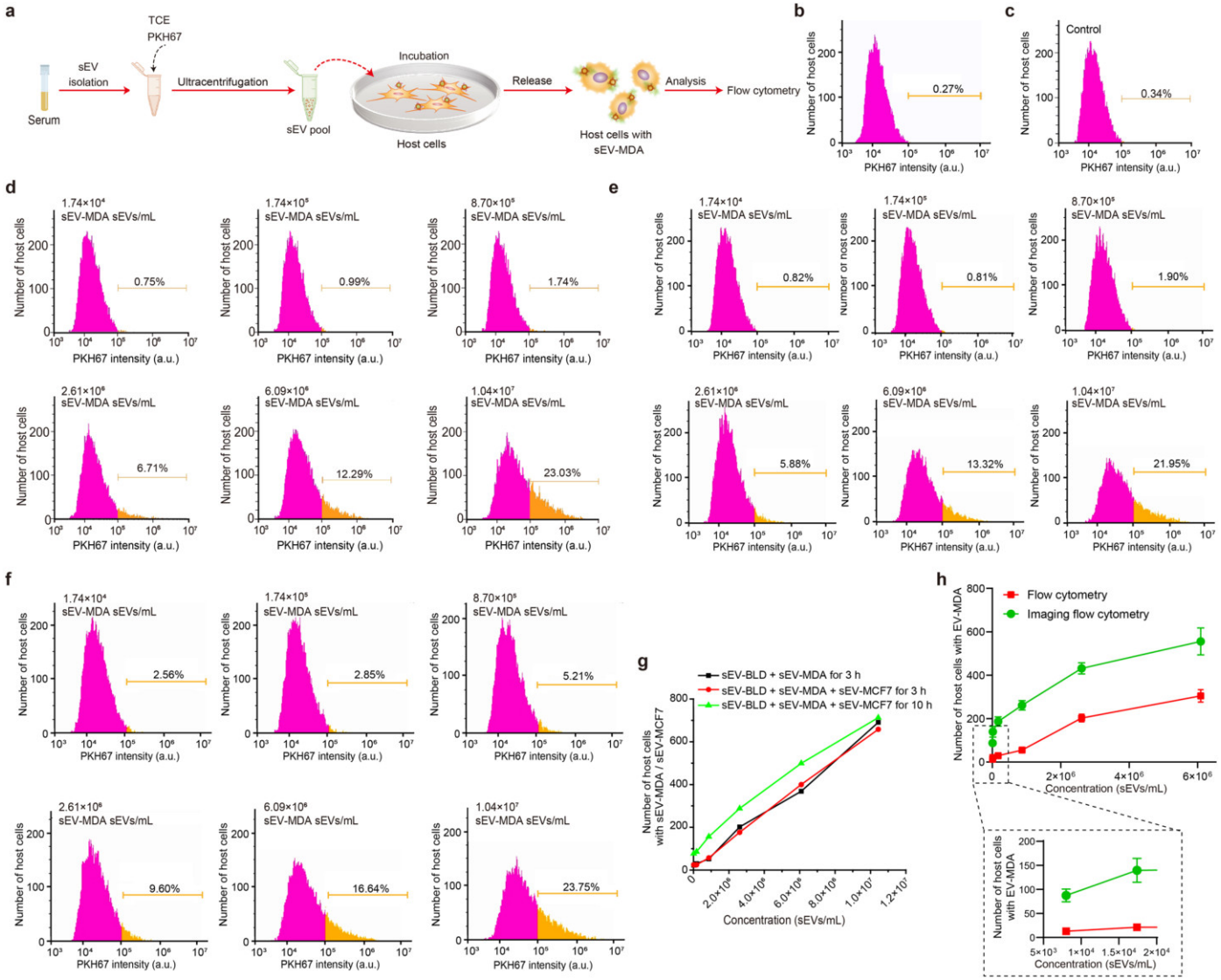

Extended Data Fig. 4 | Flow-cytometric analysis for sEV detection based on super homotypic targeting. a, Schematic of the experiment. **b**, Flow-cytometric analysis of host cells (pure MDA-MB-436 cells). MDA-MB-436 cells were suspended in 1× PBS and diluted to a concentration of 10^6 – 10^7 cells/mL without PKH67 staining. **c**, Flow-cytometric analysis of host cells (MDA-MB-436) after a 3-h incubation in FBS (control) without PKH67 staining. **d**, Flow-cytometric analysis of host cells (MDA-MB-436) after a 3-h incubation with different concentrations of sEV-MDA in serum (1 mL) containing about 4×10^8 sEVs (sEV-BLD) derived from blood cells. **e**, Flow-cytometric analysis of host cells (MDA-MB-436) after a 3-h incubation with sEV-MCF7 (2.0×10^5 sEVs/mL) and different concentrations of sEV-MDA in serum containing about 4×10^8 sEVs (sEV-BLD) derived from blood cells. **f**, Flow-cytometric analysis of host cells (MDA-MB-436) after a 10-h incubation with sEV-MCF7 (2.0×10^5 sEVs/mL) and different concentrations of sEV-MDA in serum containing about 4×10^8 sEVs (sEV-BLD) derived from blood cells. **g**, Relationship between the flow-cytometric enumeration of host cells and sEV concentration for incubation with sEV-MDA for 3 h, incubation with a mixture of sEV-MDA and sEV-MCF7 for 3 h, and incubation with a mixture of sEV-MDA and sEV-MCF7 for 10 h. **h**, Number of host cells selectively capturing sEV-MDA at different spiked concentrations in serum, detected with flow cytometry and imaging flow cytometry. Data are presented as mean ± standard deviation (n = 3 independent samples).

https://doi.org/10.1038/s41551-026-01743-2

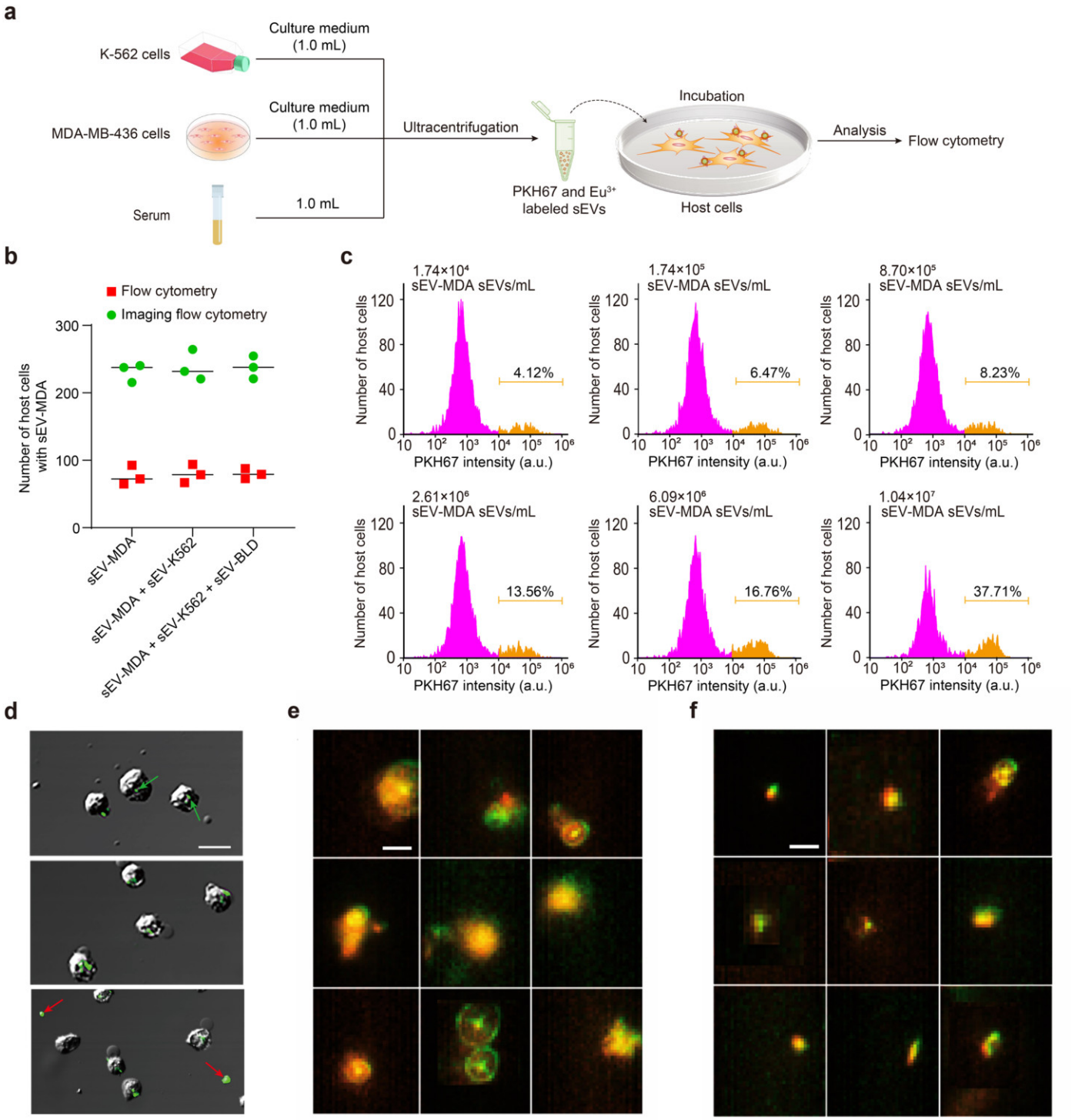

Extended Data Fig. 5 | Selective detection of sEV-MDA in the presence of sEV-K562 and imaging flow cytometry of host cells. a, Schematic of the experiment for selective detection of sEVs derived from MDA-MB-436 cells (sEV-MDA) in the presence of sEVs derived from chronic myelogenous leukaemia (sEV-K562). **b**, Number of host cells selectively capturing, isolating, and enriching sEV-MDA (1×10^7 sEVs/mL) in the presence of sEV-K562 (1×10^7 sEVs/mL) with and without sEV-BLD (4×10^8 sEVs/mL) derived from serum samples of healthy mice (n = 3 biologically independent mice). **c**, Number of host cells incubated with different concentrations of sEV-MDA, detected with imaging flow cytometry. **d**, Merged brightfield and LSCM images of MDA-MB-436 cells incubated with sEV-MDA prior to flow-cytometric analysis. Green arrows indicate cells labelled with a minimal capture number of sEVs. Red arrows indicate debris resulting in false positive events. Scale bar: 30 μm. **e, f**, Representative images of host cells labelled with sEV-MDA-Eu (green) and sEV-MCF7-Eu (red) with typical false positive (**e**) and true positive (**f**) events, acquired with imaging flow cytometry. The sEV-MDA-Eu was labelled with PKH67 (green) while sEV-MCF7-Eu was labelled with R6G (red). The mixture of sEV-MDA-Eu (green) and sEV-MCF7-Eu (red) was incubated with MDA-MB-436 cells for 3 h, and then analysed with imaging flow cytometry. Scale bars: 20 μm.

https://doi.org/10.1038/s41551-026-01743-2

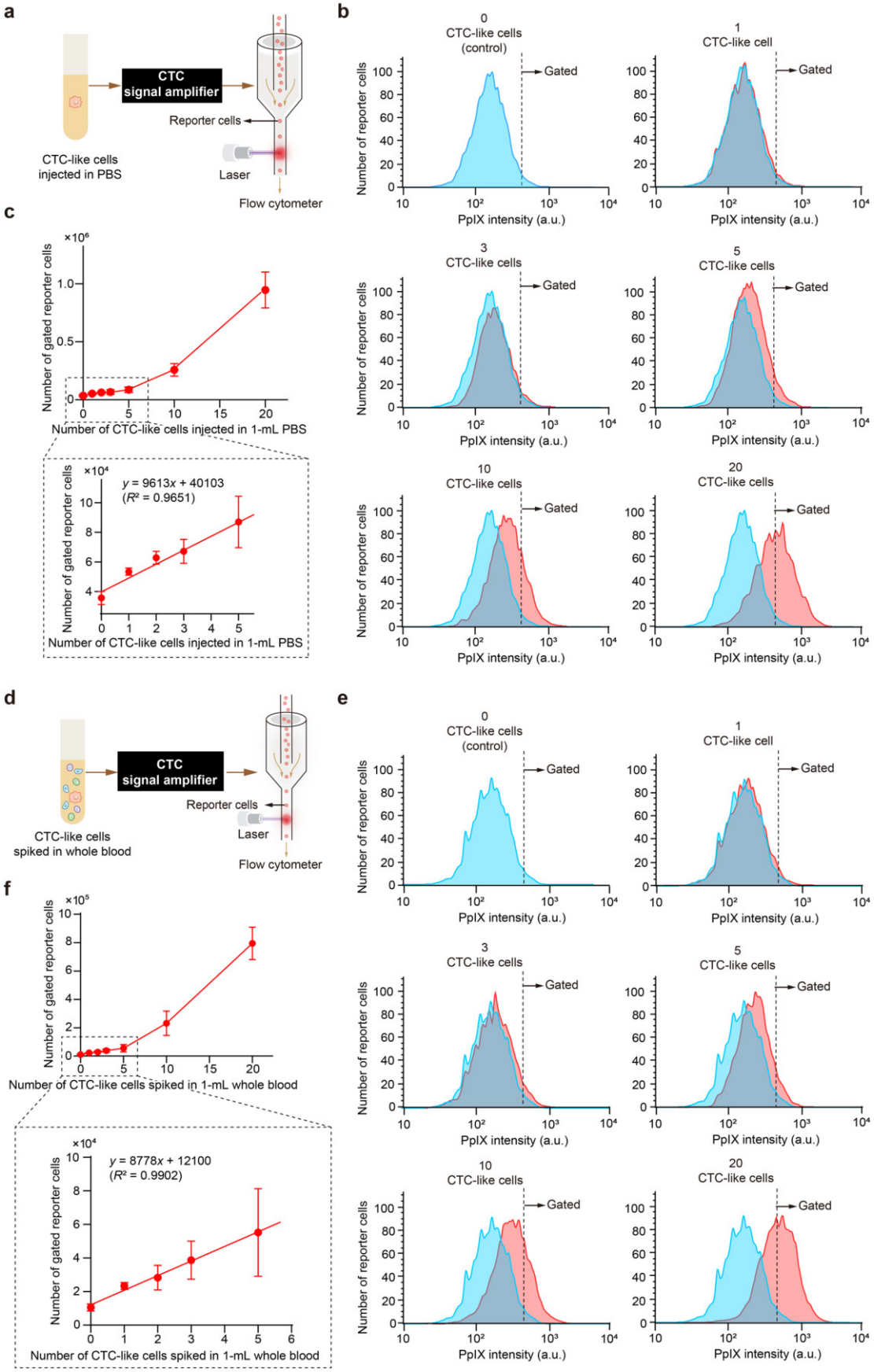

Extended Data Fig. 6 | See next page for caption.

https://doi.org/10.1038/s41551-026-01743-2

Extended Data Fig. 6 | Spike-and-recovery validation of CTC-like cells with flow cytometry. a, Schematic of the experiment. CTC-like cells were injected into 1 mL PBS and prepared for flow-cytometric evaluation. **b**, Flow cytometry of reporter cells amplifying signals from varying numbers of CTC-like cells injected in 1-mL PBS, in comparison with the control (no CTC-like cells present). Each measurement used $2{\times}10^6$ reporter cells. Dotted lines indicate gating thresholds for reporter cells. **c**, Number of gated reporter cells relative to different numbers of CTC-like cells injected in 1-mL PBS. Data are presented as mean ± standard deviation (n = 3 independent samples). The increase in the error bar size with the increasing number of CTC-like cells is due to the increasing concentration of HAL in reporter cells, following a Poisson distribution. The reason why both the slope of the linear fit and the background noise are higher than those in Fig. 7b and Extended Data Fig. 6f is the absence of PBMCs that may capture HAL-loaded sEVs. **d**, Schematic of the experiment. CTC-like cells were spiked into whole mouse blood samples (1 mL each) and prepared for flow-cytometric evaluation. **e**, Flow cytometry of reporter cells amplifying signals from varying numbers of CTC-like cells spiked in 1-mL mouse whole blood as shown in light red, in comparison with the control as shown in light blue (no CTC-like cells present). Each measurement used 2×10^6 reporter cells. Dotted lines indicate gating thresholds for reporter cells. **f**, Number of gated reporter cells relative to different numbers of CTC-like cells spiked in 1-mL whole blood samples. Data are presented as mean ± standard deviation (n = 3 independent samples). The increase in the error bar size with the increasing number of CTC-like cells is due to the increasing concentration of HAL in reporter cells, following a Poisson distribution.

https://doi.org/10.1038/s41551-026-01743-2

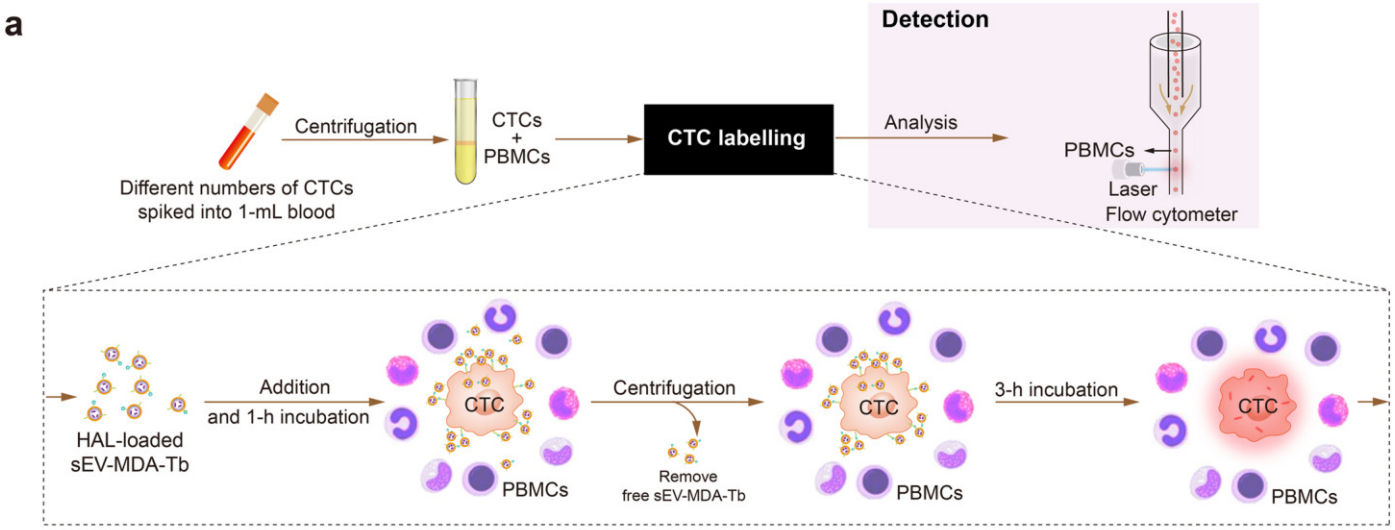

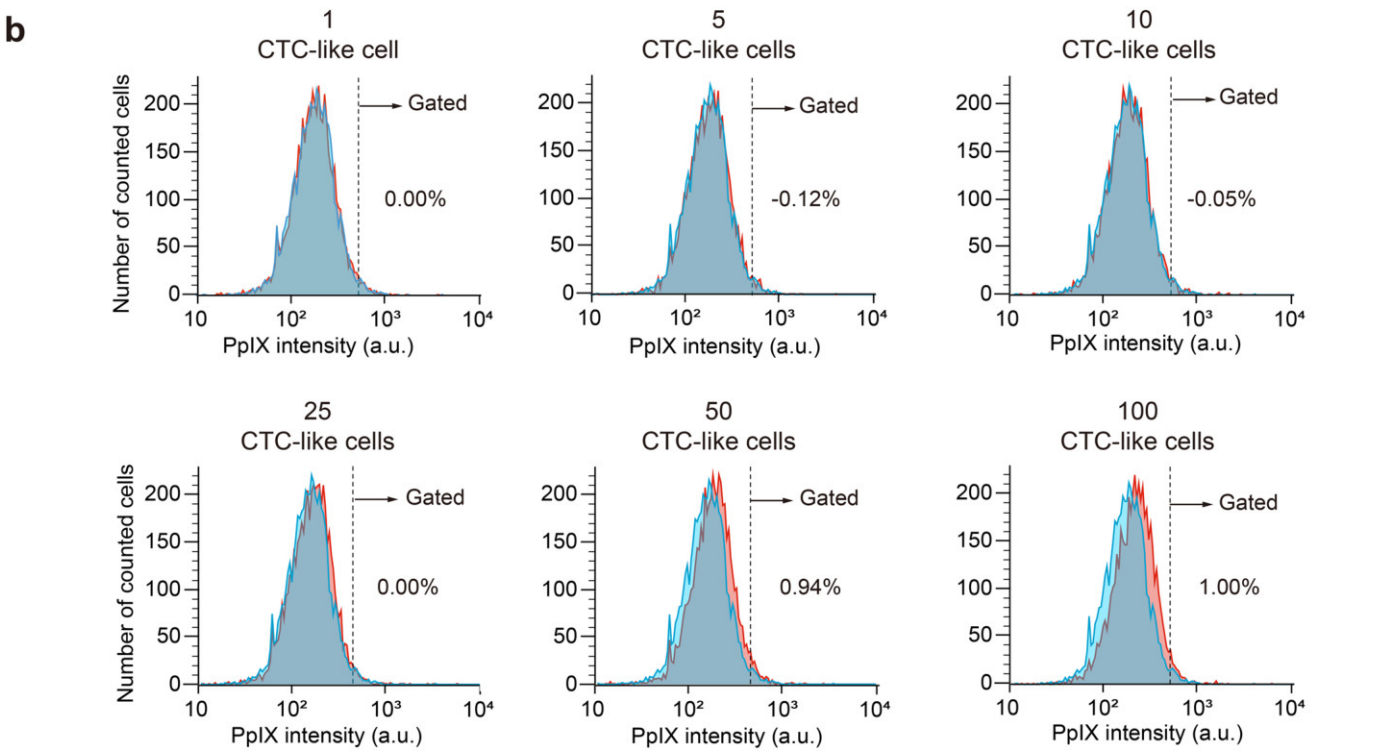

Extended Data Fig. 7 | CTC-like cell detection based on super homotypic targeting without signal amplification. a, Schematic. The detection procedure is as follows: (i) a blood sample is collected from a mouse and spiked with varying numbers of CTC-like (MDA-MB-436) cells followed by centrifugation for isolating CTC-like cells and PBMCs; (ii) the surface of sEVs derived from cells of the MDA-MB-436 cell line is engineered with Tb^{3+} ions, after loading the sEVs with HAL; (iii) the HAL-loaded surface-engineered sEVs are added to the blood sample and incubated with it so that they can specifically bind to the CTC-like cells; (iv) after removing uncaptured sEVs, an additional 3-hour incubation was conducted to convert HAL into PpIX within the CTC-like cells; (v) flow cytometry was then performed to quantify the fluorescent cell population. **b**, Flow cytometry of PBMCs with different numbers of CTC-like cells spiked into 1 mL of mouse whole blood (light red), compared with the control sample lacking CTC-like cells (light blue). Dotted lines indicate the gating thresholds used for counting fluorescently labelled cells.

https://doi.org/10.1038/s41551-026-01743-2

Extended Data Table 1 | Demographics of patients and healthy donors

Item	Category	Population	Percentage of cohort
Patients			
Sex	Female	13	100%
	Male	0	0%
Median age (range)	55 years (35-65)	-	-
TNM stage	I	3	23%
	II	8	62%
	III	2	15%
Histological grade	I	0	0%
	II	6	46%
	III	7	54%
Surgical intervention	Preoperative	4	31%
	Postoperative	9	69%
Adjuvant therapy	Chemotherapy	13	100%
	Radiation therapy	6	46%
	Targeted therapy	2	15%
Healthy donors			
Sex	Female	13	100%
	Male	0	0%

https://doi.org/10.1038/s41551-026-01743-2

Extended Data Table 2 | Histopathological reports for the TNBC patients

Patient No.	ER/PR/HER2 status	Key histopathological report
1	$ER^-/PR^-/HER2^-$	Invasive ductal carcinoma. No clear nerve or vascular invasion was observed.
2	$ER^-/PR^-/HER2^-$	Invasive ductal carcinoma. Fibroadenoma formation was observed in the breast after surgery, and no cancer tissue metastasis was found in the axillary lymph nodes.
3	$ER^-/PR^-/HER2^-$	Invasive ductal carcinoma. No vascular invasion was observed, and no cancer metastasis was found in the lymph nodes.
4	$ER^-/PR^-/HER2^-$	Invasive ductal carcinoma. Cancer metastasis in axillary lymph nodes was observed.
5	$ER^-/PR^-/HER2^-$	Invasive lobular carcinoma, accompanied by differentiation of sweat glands.
6	$ER^-/PR^-/HER2^-$	Invasive ductal carcinoma, accompanied by intermediate grade ductal carcinoma in situ.
7	$ER^-/PR^-/HER2^-$	Invasive ductal carcinoma. There was cancer metastasis in the axillary lymph nodes and fibroadenoma in the right breast.
8	$ER^-/PR^-/HER2^-$	Invasive ductal carcinoma. No clear vascular cancer thrombus was observed.
9	$ER^-/PR^-/HER2^-$	Invasive ductal carcinoma, accompanied by interstitial fibrosis. No vascular cancer thrombus or nerve invasion was observed.
10	$ER^-/PR^-/HER2^-$	Invasive ductal carcinoma. No vascular cancer thrombus was observed.
11	$ER^-/PR^-/HER2^-$	Invasive ductal carcinoma, accompanied by perilobular lymphatic tissue infiltration.
12	$ER^-/PR^-/HER2^-$	Invasive ductal carcinoma, accompanied by partial ductal epithelial hyperplasia in the right breast tissue.
13	$ER^-/PR^-/HER2^-$	Invasive ductal carcinoma, accompanied by high-grade ductal carcinoma in situ.

nature portfolio

Corresponding author(s): Keisuke Goda

Last updated by author(s): Mar 24, 2026

Reporting Summary

Nature Portfolio wishes to improve the reproducibility of the work that we publish. This form provides structure for consistency and transparency in reporting. For further information on Nature Portfolio policies, see our Editorial Policies and the Editorial Policy Checklist.

Statistics

For all statistical analyses, confirm that the following items are present in the figure legend, table legend, main text, or Methods section.

n/a	Confirmed	
☐	☒	The exact sample size (*n*) for each experimental group/condition, given as a discrete number and unit of measurement
☐	☒	A statement on whether measurements were taken from distinct samples or whether the same sample was measured repeatedly
☐	☒	The statistical test(s) used AND whether they are one- or two-sided *Only common tests should be described solely by name; describe more complex techniques in the Methods section.*
☒	☐	A description of all covariates tested
☒	☐	A description of any assumptions or corrections, such as tests of normality and adjustment for multiple comparisons
☐	☒	A full description of the statistical parameters including central tendency (e.g. means) or other basic estimates (e.g. regression coefficient) AND variation (e.g. standard deviation) or associated estimates of uncertainty (e.g. confidence intervals)
☐	☒	For null hypothesis testing, the test statistic (e.g. *F*, *t*, *r*) with confidence intervals, effect sizes, degrees of freedom and *P* value noted *Give P values as exact values whenever suitable.*
☒	☐	For Bayesian analysis, information on the choice of priors and Markov chain Monte Carlo settings
☒	☐	For hierarchical and complex designs, identification of the appropriate level for tests and full reporting of outcomes
☒	☐	Estimates of effect sizes (e.g. Cohen's *d*, Pearson's *r*), indicating how they were calculated

Our web collection on statistics for biologists contains articles on many of the points above.

Software and code

Policy information about availability of computer code

Data collection	CytExpert was used with CytoFLEX LX for the data collection of flow cytometry. Olympus Fluoview was used for data collection of laser scanning confocal microscopy. LabVIEW2016 was used for data collection of imaging flow cytometry. Western blots were captured using iBright CL1500 Imaging System.
Data analysis	Python 3 was used for image preprocessing in imaging flow cytometry. ImageJ Fiji was used for image analysis in laser scanning confocal microscopy. Origin (2021) and Graphpad Prism (V8) were used for statistical analysis. FlowJo (v10.8.1) was used for analysis of FACS data.

For manuscripts utilizing custom algorithms or software that are central to the research but not yet described in published literature, software must be made available to editors and reviewers. We strongly encourage code deposition in a community repository (e.g. GitHub). See the Nature Portfolio guidelines for submitting code & software for further information.

Data

Policy information about availability of data

All manuscripts must include a data availability statement. This statement should provide the following information, where applicable:

- Accession codes, unique identifiers, or web links for publicly available datasets
- A description of any restrictions on data availability
- For clinical datasets or third party data, please ensure that the statement adheres to our policy

All relevant data supporting the findings of this study are available within the Article, Extended Data, Supplementary Information or Source Data files. Source data are provided with this paper.

Research involving human participants, their data, or biological material

Policy information about studies with human participants or human data. See also policy information about sex, gender (identity/presentation), and sexual orientation and race, ethnicity and racism.

Reporting on sex and gender	Sex was reported. Only female participants with TNBC and healthy subjects were included in this study. Data on gender identity were not collected.
Reporting on race, ethnicity, or other socially relevant groupings	This study did not use race, ethnicity or other socially relevant groupings.
Population characteristics	The TNBC cohort comprised 13 female patients with a median age of 55 years (range: 35–65). All patients were histopathologically confirmed to have TNBC, with disease grades distributed as follows: Grade I (0%), Grade II (46%), and Grade III (54%).
Recruitment	Participants were consecutively screened and recruited from clinical sites. TNBC patients were eligible if they had a pathologically confirmed diagnosis of TNBC ($ER^-/PR^-/HER2^-$), with typical histopathological features such as invasive ductal carcinoma or invasive lobular carcinoma. Patients who had received prior treatments, including surgery, chemotherapy, radiotherapy, or targeted therapy, were permitted. Key exclusion criteria for all participants was a history of other cancers. Healthy subjects with no personal history of cancer were recruited separately.
Ethics oversight	The study for the TNBC cohort was approved by the ethics committees of Nanjing Hospital of Chinese Medicine (No. KY2024088) and China Pharmaceutical University (No. 220201299). Consent was obtained directly from all participants.

Note that full information on the approval of the study protocol must also be provided in the manuscript.

Field-specific reporting

Please select the one below that is the best fit for your research. If you are not sure, read the appropriate sections before making your selection.

☒ Life sciences ☐ Behavioural & social sciences ☐ Ecological, evolutionary & environmental sciences

For a reference copy of the document with all sections, see nature.com/documents/nr-reporting-summary-flat.pdf

Life sciences study design

All studies must disclose on these points even when the disclosure is negative.

Sample size	5×10^3 to 1×10^4 items were collected for each cell sample in flow cytometric analysis. 3×10^3 to 3×10^4 images were collected for each cell sample in imaging flow cytometric analysis. Serum samples from 10 healthy mice and 10 TNBC tumor-bearing mice per condition were analyzed for validation of extreme-precision sEV detection. Blood samples from 5 healthy mice and 5 TNBC tumor-bearing mice per condition were analyzed for validation of extreme-precision CTC detection. Serum samples from 13 healthy subjects and 13 TNBC patients were analyzed for validation of extreme-precision sEV detection. Blood samples from 13 healthy subjects and 13 TNBC patients were analyzed for validation of extreme-precision CTC detection.
Data exclusions	5×10^3 to 1×10^4 items were randomly selected for data analysis of flow cytometry. 3×10^3 to 3×10^4 images were randomly selected for data analysis of imaging flow cytometry. Gating was applied for FACS data. No mice and patients were excluded from the study.
Replication	The reproducibility of cell experiment is illustrated in Fig. 5f, 7b, 7c and 7e, and Extended Data Fig. 4h, 6c and 6f.
Randomization	For blood experiments, animals were randomly assigned to different groups.
Blinding	All mice were randomized and their selection for injection or blood collection was conducted blindly.

Reporting for specific materials, systems and methods

We require information from authors about some types of materials, experimental systems and methods used in many studies. Here, indicate whether each material, system or method listed is relevant to your study. If you are not sure if a list item applies to your research, read the appropriate section before selecting a response.

Materials & experimental systems

n/a	Involved in the study
☐	☒ Antibodies
☐	☒ Eukaryotic cell lines
☒	☐ Palaeontology and archaeology
☐	☒ Animals and other organisms
☒	☐ Clinical data
☒	☐ Dual use research of concern
☒	☐ Plants

Methods

n/a	Involved in the study
☒	☐ ChIP-seq
☐	☒ Flow cytometry
☒	☐ MRI-based neuroimaging

Antibodies

Antibodies used	SNA-FITC, Sambucus Nigra (Elderberry Bark) Lectin (SNA, EBL) labeled with fluorescein (Thermo Fisher, L32479, 1:400), was utilized to label MCF-7 and MDA-MB-436 cells. TSG101, Alix, and CD63 antibodies were used for WB analysis of small extracellular vesicle proteins: Rabbit anti-TSG101 (Abcam, ab125011, Clone EPR7130(B), 1:1000), Rabbit anti-Alix (Abcam, ab186429, Clone EPR15314, 1:1000), Rabbit anti-CD63 (Cell Signaling Technology, 52090, Clone E1W3T, 1:1000). In addition, secondary antibody was used for WB: anti-rabbit IgG (HRP linked, Cell Signaling Technology, 7074, 1:5000).
Validation	We follow the manufactures' instruction to use the above listed antibodies. Additional validation was done by the use of control cells.

Eukaryotic cell lines

Policy information about cell lines and Sex and Gender in Research

Cell line source(s)	MCF-7, MDA-MB-436, B16, HepG2, THLE-2 and K562 cells are all deprived from ATCC (Manassas, VA, USA).
Authentication	All cell lines were authenticated by the vendor by morphology check and growth curve analysis. The cell lines were purchased from commercial vendors listed above.
Mycoplasma contamination	Cell lines were routinely tested and found negative for mycoplasma infection by the venders.
Commonly misidentified lines (See ICLAC register)	No commonly misidentified cell lines were used.

Animals and other research organisms

Policy information about studies involving animals; ARRIVE guidelines recommended for reporting animal research, and Sex and Gender in Research

Laboratory animals	BALB/c nude mice (5 weeks old, female, inbred strain, substrain BALB/cAnNCrl-nu, obtained from Beijing Vital River Laboratory Animal Technology Co., Ltd.). The mice were housed under specific pathogen-free conditions, with a 12-h light/dark cycle, ambient temperature of 22 ± 2 °C, and relative humidity of 50 ± 10%.
Wild animals	No wild animals were used in the study.
Reporting on sex	All mice were female.
Field-collected samples	No field-collected samples were used in this study.
Ethics oversight	All experiment animals were housed with Pharmaceutical Animal Experimental Center at China Pharmaceutical University under specific pathogen-free (SPF) conditions and received care in accordance with ethical requirements for animal welfare (No. 220201299).

Note that full information on the approval of the study protocol must also be provided in the manuscript.

Flow Cytometry

Plots

Confirm that:

☒ The axis labels state the marker and fluorochrome used (e.g. CD4-FITC).

☒ The axis scales are clearly visible. Include numbers along axes only for bottom left plot of group (a 'group' is an analysis of identical markers).

☒ All plots are contour plots with outliers or pseudocolor plots.

☒ A numerical value for number of cells or percentage (with statistics) is provided.

Methodology

Sample preparation	The cell concentration was adjusted to 10^6-10^7 cells/mL by dilution with PBS
Instrument	Beckman CytoFLEX LX
Software	Beckman CytExpert
Cell population abundance	The cell concentration was adjusted to 10^6 to 10^7 cells/mL by dilution with PBS for flow cytometric analysis.
Gating strategy	FSC-A x FSC-H data was used for eliminate aggregated cells. The percentage of positive cells was determined by evaluating the fluorescence intensity of the cells.

☒ Tick this box to confirm that a figure exemplifying the gating strategy is provided in the Supplementary Information.